

HOT ELECTROMAGNETIC OUTFLOWS I: ACCELERATION AND SPECTRA

MATTHEW RUSSO

Department of Physics, University of Toronto, 60 St. George St., Toronto, ON M5S 1A7, Canada.

CHRISTOPHER THOMPSON

Canadian Institute for Theoretical Astrophysics, 60 St. George St., Toronto, ON M5S 3H8, Canada.

To be published in the Astrophysical Journal

ABSTRACT

The theory of cold, relativistic, magnetohydrodynamic outflows is generalized by the inclusion of an intense radiation source. In some contexts, such the breakout of a gamma-ray burst jet from a star, the outflow is heated to a high temperature at a large optical depth. Eventually it becomes transparent and is pushed to a higher Lorentz factor by a combination of the Lorentz force and radiation pressure. We obtain its profile, both inside and outside the fast magnetosonic critical point, when the poloidal magnetic field is radial and monopolar. Most of the energy flux is carried by the radiation field and the toroidal magnetic field that is wound up close to the rapidly rotating engine. Although the entrained matter carries little energy, it couples the radiation field to the magnetic field. Then the fast critical point is pushed inward from infinity and, above a critical radiation intensity, the outflow is accelerated mainly by radiation pressure. We identify a distinct observational signature of this hybrid outflow: a hardening of the radiation spectrum above the peak of the seed photon distribution, driven by bulk Compton scattering. The non-thermal spectrum – obtained by a Monte Carlo method – is most extended when the Lorentz force dominates the acceleration, and the seed photon beam is wider than the Lorentz cone of the MHD fluid. This effect is a generic feature of hot, magnetized outflows interacting with slower relativistic material. It may explain why some GRB spectra appear to peak at photon energies above the original Amati et al. scaling. A companion paper addresses the case of jet breakout, where diverging magnetic flux surfaces yield strong MHD acceleration over a wider range of Lorentz factor.

Subject headings: MHD — plasmas — radiative transfer — scattering — gamma rays: stars

1. INTRODUCTION

Some astrophysical sources release energy at prodigious rates, as a result of their extreme magnetism and/or rotation. Gamma-ray bursts (GRBs) and soft gamma repeater flares are familiar examples, but the range of possibilities extends to rapidly rotating white dwarfs formed in binary mergers, or young and hot magnetars. The ‘engine’ generates an outflow that contains both an intense magnetic field and also a powerful flow of radiation. A gamma-ray burst jet becomes hot as it works its way through a preceding layer of stellar material, as in the collapsar model (MacFadyen & Woosley 1999); or interacts with a powerful neutron-rich wind that was generated in the initial stages of a binary merger (e.g. Dessart et al. 2009). A blackbody component is also expected to be carried outward from the engine itself even in the absence of jet interaction (Goodman 1986).

We have previously argued that the full GRB phenomenon cannot be captured by ‘thermal fireballs’ (Goodman 1986; Shemi & Piran 1990), or ‘Poynting-dominated outflows’ (Lyutikov & Blandford 2003) alone. Instead both components are needed: thermal photons to provide seeds for gamma-ray emission, and large-scale magnetic fields to drive the outflow and then trigger non-thermal activity and fast variability (Thompson 1994; Meszaros & Rees 1997; Drenkhahn & Spruit 2002; Thompson 2006; Giannios & Spruit 2007; Zhang & Yan 2011). In some other circumstances, such as white dwarf merger remnants, the photon luminosity is bounded by the Eddington value, but the spindown luminosity can be vastly greater. (It is, of course, possible to find situations in which this inequality is reversed: the photon energy flux in giant magnetar flares is strong enough to pull some magnetic flux away from the star, but the total energy flux is probably dominated by photons.)

1.1. Acceleration

Our first interest here is in how such a ‘hot electromagnetic outflow’ is accelerated. We focus on stationary, axisymmetric flows in the ideal MHD limit, but add a radiation field with a prescribed source radius that can have arbitrary size with respect to the light cylinder. The inertia of the magnetic field dominates that of the matter to which it is tied, so that the outflow can achieve relativistic speeds. The magnetofluid is accelerated by two mechanisms: the Lorentz force (which operates in cold MHD winds); and scattering off the radiation field (which operates in thermal fireballs).

In the optically thin regime, the radiation field is self-collimating, so that a relativistically moving frame can be defined in which the radiation exerts a vanishing net force on the matter. Radiation pressure dominates matter pressure, and with the possible exception of a small region close to the engine, the radiation temperature lies far below the rest energy of the advected particles. The outflow can therefore be assumed cold outside the transparency surface, and scattering operates in the Thomson limit. In this first paper, we follow Goldreich & Julian (1970) in restricting the poloidal magnetic field to a monopolar geometry. This limits the efficiency of MHD acceleration (the fast critical point of the cold MHD flow sits at infinity). A much stronger Lorentz force can arise through differential decollimation of magnetic flux surfaces (e.g. Tchekhovskoy et al. 2009), but even

then some parts of a cold MHD outflow may not have the requisite geometry. A companion paper considers jet geometries and allows for differential decollimation of the jet with respect to the radiation field (Russo & Thompson 2012, paper II).

The efficiency of radiative acceleration outside the fast magnetosonic point was noted by Thompson (2006) in the context of GRBs. Previous work by Li et al. (1992) and Beskin et al. (2004) considered the interaction of a relativistic MHD outflow with a quasi-isotropic radiation field. In a first approximation, the outflowing matter feels a net drag force. Beskin et al. (2004) focused on a slightly decollimating outflow with fast MHD acceleration, and analysed the influence of radiation drag in integral form through the changes imparted to the energy and angular momentum. They considered changes in the shape of the magnetic surfaces, and therefore in the MHD acceleration rate, imparted by the radiation field, but the first-order effect addressed in this paper – the outward acceleration due to the strong radial anisotropy of the radiation field – was absent in their calculations.

We focus on time-independent outflows, because acceleration by radiation pressure becomes important before effects associated with the radial structure of the flow. The acceleration of a magnetized slab in planar geometry was studied numerically by Granot et al. (2011). The slab is initially static; its mean Lorentz factor quickly reaches $\sigma_0^{1/3}$, where σ_0 is the initial magnetization, and then continues to grow. This effect may be relevant to GRBs after a jet has made a transition to a planar geometry at a distance $r \gtrsim c\Delta t \sim 3 \times 10^{11}(\Delta t/10 \text{ s}) \text{ cm}$, where Δt is the duration of the prompt phase. If the shell is already moving relativistically, only the outermost fraction $\sim 1/2\Gamma^2$ of the shell will experience this type of acceleration. The interaction of this thin layer with an external plasma shell, which absorbs momentum from the magnetic field (e.g. Thompson 2006), must also be taken into account. Typically the bulk of the shell receives momentum from the radiation field before it comes into causal contact.

We do not address how the outflow might accelerate below its scattering photosphere. For example, periodic reversals of a toroidal field might induce magnetic reconnection, break the degeneracy between magnetic pressure gradient and curvature forces, and thereby induce a net outward acceleration (Drenkhahn & Spruit 2002). The high efficiency claimed for this mechanism depends on neglecting the input of enthalpy, and therefore inertia, into the magnetofluid as the magnetic field reconnects. When an enthalpy source term is included, one only obtains relativistic bulk motion if a high fraction of the unsigned magnetic flux is removed by reconnection. This requires, at a minimum, that the net (signed) magnetic flux carried by the outflow is small compared with the unsigned flux, and that the non-radial magnetic field maintains a strictly uniform (e.g. toroidal) direction across current sheets. Our focus here and in paper II is therefore on ideal MHD effects.

1.2. Non-thermal Spectrum

The second focus of this paper is on the non-thermal spectrum of photons that are scattered by the outflowing matter. We ignore any effects of internal dissipation in the outflow, and focus purely on the spectral signature of bulk relativistic motion. We find a broad and flat extension of the seed spectrum when the outflow is rapidly accelerated by the Lorentz force, so that the seed photon beam is wider than the Lorentz cone of the MHD outflow. The smoothness of the scattered spectrum – in particular, the presence or absence of a residual bump at the seed thermal peak – is shown to depend on the net optical depth that is seen by the broader, unscattered photon beam.

Existing calculations of non-thermal ‘photospheric’ emission from GRB outflows (Giannios 2006; Beloborodov 2011) generally assume that the Lorentz factor of the outflow has saturated at the transparency surface, as do calculations of the low-frequency spectral tail of thermal photospheres observed at oblique angles (e.g. Pe’er 2008; Lazzati et al. 2011). We broaden this approach by noting that locking between the advected thermal photons and the relativistic outflow will be broken in the presence of a somewhat slower component of the outflow. For example, material with a Lorentz factor $\sim 3-5$ times smaller than the magnetofluid would be present as the result of the interaction of a jet with a star (Thompson 2006). In a neutron star binary merger, a relativistic magnetofluid could interact with a sub-relativistic, neutron-rich wind (Bucciantini et al. 2012). The slower material scatters advected X-ray photons into a broader beam, which continues to interact strongly with the faster magnetofluid even at low optical depth. It has long been realized that relativistic material moving into an isotropic bath of very low-frequency (optical-UV) photons will upscatter them as it *loses* energy to Compton drag (e.g. Sikora et al. 1994; Ghisellini et al. 2000). In that case a spectral slope $F_\nu \sim \nu^{-1/2}$ is generated by the decaying peak energy of the upscattered photons – a different effect from that considered here, and a spectrum somewhat softer than that observed in the low-energy tails of GRBs.

1.3. Plan

The plan of the paper is as follows. Section 2 explains the efficiency of radiation-driven acceleration beyond the fast magnetosonic point, and explains further our critique of acceleration by magnetic reconnection. The relativistic wind equations including radiation pressure are described in Section 3, and in Section 4 they are specialized to a monopole magnetic field. The flow properties near the fast critical point are analysed and the numerical method described. Numerical results are presented in Section 5. The spectrum of scattered photons is calculated in Section 6 by a Monte Carlo method, and the low- and high-frequency components of the spectrum discussed in the context of GRBs. Our results are summarized in Section 7, and the effect of rotation in the photon source is briefly discussed in Appendix A.

2. ACCELERATION OF MAGNETICALLY DOMINATED FLOWS BY RADIATION PRESSURE

The outflow may be divided into an inner, optically thick part, in which the radiation field is effectively tied to the matter; and an outer part through which the radiation can flow almost unimpeded.¹ Within this outer transparent zone, the radiation field becomes progressively more collimated with increasing distance from the engine. Even at the transparency radius, it can remain so intense as to push matter to much higher Lorentz factors than were achieved by hydromagnetic stresses operating in the inner zone.

¹ A hard radiation spectrum, extending above $m_e c^2$ in the frame of the ambient material, can trigger an e^+e^- cascade outside the photosphere of a *relativistic* outflow (Thompson & Madau 2000; Beloborodov 2002). We ignore the effect of pair creation on the optical depth in this paper.

The radiation has a positive accelerating effect outside the scattering photosphere if the terminal Lorentz factor Γ_∞ of the matter exceeds the Lorentz factor $\Gamma(r_\tau)$ at the transparency radius r_τ . The intensity of the radiation field is measured by the compactness, which here is normalized to the mean mass \bar{m} per scattering charge:

$$\chi(r_\tau) = \frac{\sigma_T}{\bar{m}c^3 r_\tau} \frac{dL_\gamma}{d\Omega}. \quad (1)$$

Here L_γ is the isotropic radiation luminosity, and σ_T is the Thomson cross-section (we only consider classical electron scattering in this paper). Defining the scattering optical depth

$$\tau_{\text{es}} = \int \Gamma \frac{\rho(r)}{\bar{m}} (1 - \beta_r) \sigma_T dr \quad (2)$$

in a slowly rotating outflow with speed $\beta_r c$ and proper mass density ρ , the surface $\tau_{\text{es}} = 1$ can be related to the flux of rest mass \dot{M} ,

$$r_\tau \simeq \frac{\sigma_T}{6\Gamma^2(r_\tau)\bar{m}c} \frac{d\dot{M}}{d\Omega}. \quad (3)$$

The magnetization of a relativistic outflow can be expressed in terms of the ratio of Poynting flux to rest energy flux, which is, far outside the speed of light cylinder,

$$\frac{dL_P}{d\Omega} \sim \frac{B_\phi^2}{4\pi} r^2 c \simeq \sigma \frac{d\dot{M}}{d\Omega} c^2. \quad (4)$$

The magnitude of σ in GRB outflows is unknown, but there are a number of reasons to expect a range of values within different components of the same outflow. The simplest case – but perhaps not the most relevant for classical GRBs – involves a rapidly rotating nascent magnetar, whose wind can achieve a magnetization $\sim 10^3$ at late times after an early dirty wind phase (Metzger et al. 2011).

At $r = r_\tau$, one therefore has the relation between photon compactness and magnetization,

$$\chi(r_\tau) \sim 6\Gamma^2(r_\tau) \frac{dL_\gamma/d\Omega}{dL_P/d\Omega} \sigma. \quad (5)$$

The terminal Lorentz factor of a radiation-driven baryonic wind is (see Section 5.2)

$$\Gamma_\infty(r_\tau) \sim [\chi(r_\tau)\Gamma(r_\tau)]^{1/4} = \left[6\Gamma^3(r_\tau) \frac{dL_\gamma/d\Omega}{dL_P/d\Omega} \sigma \right]^{1/4}. \quad (6)$$

Hence the outflow emerges into transparency below this limiting Lorentz factor if

$$\frac{\Gamma(r_\tau)}{\Gamma_\infty} = \left[\frac{\Gamma(r_\tau)}{6(L_\gamma/L_P)\sigma} \right]^{1/4} < 1, \quad (7)$$

corresponding to $\Gamma(r_\tau) \lesssim \sigma$ in a hot outflow with $L_\gamma \sim L_P$. Radiation plays a key role in accelerating the outflow when this bound is satisfied.

2.1. Strong Radiative Acceleration Outside the Fast Critical Point

An essential feature of a *steady* magnetohydrodynamic (MHD) flow is that the equation for the fluid speed, obtained by combining the continuity and momentum equations, becomes singular where it matches a normal mode of the fluid. In the absence of significant matter pressure, the relevant normal modes are the Alfvén mode and the fast mode.

In a relativistic outflow, the inertia of the advected toroidal magnetic field rapidly becomes insignificant outside the fast critical point. Here we consider the case where the poloidal magnetic flux surfaces do not experience the differential bending needed for efficient MHD acceleration. Then, when the radiative force is strong enough to provide significant acceleration at the fast point, it also controls the terminal acceleration of the outflow, as if the magnetic field were not present. In spite of this, the Poynting flux carried by the magnetic field can continue to dominate the kinetic energy flux: the matter acts as a couple between the radiation field and the magnetic field (Thompson 2006).

To see this, focus on the zone far outside the Alfvén critical point. The solution to the induction equation is (Ferraro 1937)

$$\frac{B_\phi}{B_r} = \frac{v_\phi - \Omega_f r \sin \theta}{v_r}, \quad (8)$$

where Ω_f is the rotational angular frequency of the magnetic footpoint at the boundary of the engine, and is constant along a magnetic flux surface. Equation (8) implies a uniform rate of transport of toroidal magnetic flux

$$\dot{\Phi}_\phi = v_r r B_\phi \simeq -\Omega \sin \theta r^2 B_r = \text{const}, \quad (9)$$

since the toroidal velocity has decreased to $v_\phi \ll v_r \simeq c$. We now allow an external (e.g. radiation) force to be applied to the fluid while imposing this constraint, as well as the constancy of mass flux

$$\frac{d\dot{M}}{d\Omega} = \Gamma \rho v_r r^2 = \text{const.} \quad (10)$$

The change in the radial energy flux is, at a fixed radius,

$$\delta T_{rr} = \delta \left(\Gamma^2 \rho c^2 v_r + \frac{E_\theta B_\phi}{4\pi} c \right) = \frac{1}{r^2} \delta \left(\frac{d\dot{M}}{d\Omega} c^2 - \dot{\Phi}_\phi^2 \frac{1}{v_r} \right) \simeq \frac{\delta \Gamma}{r^2} \left(\frac{d\dot{M}}{d\Omega} c^2 - \frac{\dot{\Phi}_\phi^2}{\Gamma^3 c} \right). \quad (11)$$

The right-hand-side here is singular at the fast point, where

$$\Gamma^3 = \Gamma_c^3 = \frac{\dot{\Phi}_\phi^2}{c^3 d\dot{M}/d\Omega} = \sigma. \quad (12)$$

The (toroidal) magnetic field dominates the inertia of the outflow in between the Alfvén and fast points, but the small flux of ordinary matter dominates outside the fast point.

Our main focus is on flows that are sub-fast magnetosonic at the transparency surface, and are accelerated through the critical point by the radiation force as well as the Lorentz force. For our adopted field geometry, this occurs when $\Gamma(r_\tau) \lesssim \sigma^{1/3}$, and requires a strongly magnetized outflow.

A second type of flow is super-fast magnetosonic at the transparency surface, having already been accelerated through the critical point, $\Gamma(r_\tau) \gtrsim \sigma^{1/3}$. The dominant acceleration mechanism outside the photosphere then depends on the poloidal field geometry. When the poloidal flux surfaces do not diverge from each other, the case studied in this paper, the Lorentz force freezes out and the remaining acceleration is by the radiation force. However, in a jet geometry there is a much more extended competition between MHD and radiation stresses outside the fast critical point, as we discuss in paper II.

2.2. Insensitivity to Flow Structure Near the Alfvén Critical Point

Since the Alfvén mode has the lower speed, its critical point sits closer to the rotating ‘engine’. Inside the Alfvén critical point, the magnetic field lines are effectively rigid and guide the outflow of matter and radiation. Outside, the rotation of the engine causes the magnetic field lines to be bent back into a Parker spiral, and the magnetic field is mainly toroidal. After a choice is made for the poloidal field profile, we wish to test the *insensitivity* of the large-distance flow solution to details close to the Alfvén point. In fact, we obtain an essentially unique outer solution without explicitly requiring it to pass through the Alfvén point. If the solution were not unique in this way, it would be suspect: the magnetic field configuration near the Alfvén point maps directly onto the engine, and details of the inner flow solution depend, in turn, on details of plasma heating close to the engine.

2.3. Bulk Acceleration by Magnetic Reconnection: A Critique

The acceleration of a cold, spherical MHD outflow is inefficient due to a cancellation between the magnetic pressure gradient and curvature forces. Rather than considering deviations from radial flow, Drenkhahn & Spruit (2002) suggest that reconnection of a reversing toroidal magnetic field would convert Poynting flux to a large-scale relativistic expansion. Inside the scattering photosphere, they impose conservation of energy flux per steradian,

$$\frac{dL}{d\Omega} = r^2 \Gamma^2 v_r \left[h + \frac{(B_\phi/\Gamma)^2}{4\pi} \right]. \quad (13)$$

Here $h \simeq \rho c^2$ is the bulk-frame enthalpy per unit volume, ρ is the proper rest-mass density, and B_ϕ/Γ the bulk-frame toroidal magnetic field. A sink term for the magnetic flux is imposed, $c \partial_r (r B_\phi v_r) = -r B_\phi v_r / \tau$, but no corresponding source of h . With these assumptions, the dissipation of Poynting flux must be compensated by a growth in kinetic energy. A small decrease in Poynting flux corresponds to a large increase in Γ in a cold, high- σ outflow.

More realistically, reconnection heats the particles, and in a high- σ outflow there is a large increase in the particle inertia. Even allowing for rapid radiative cooling, the photons are trapped by the outflow, and

$$\delta h \sim -\delta \left[\frac{(B_\phi/\Gamma)^2}{8\pi} \right]. \quad (14)$$

Reconnection also creates a radial magnetic field, through the appearance of multiple magnetic X-points. The inertia of this small-scale magnetic field also dominates the particle rest mass. Taking both of these effects into account, one sees that dissipation of even half the magnetic energy can generate only mildly relativistic bulk motion.

3. OUTFLOW EQUATIONS

Given the technical challenge involved in adding the radiation force, we are forced to make simplifying assumptions about the angular distribution of the poloidal magnetic flux. In this first paper we follow Goldreich & Julian (1970) in allowing the magnetic field to bend in the toroidal but not the poloidal directions – i.e., the poloidal field is purely radial. This approximation is, in fact, increasingly well justified for very intense radiation fields, e.g., those which are strong enough to force open magnetic

field lines inside the speed of light cylinder. It should also hold with reasonable accuracy close to the magnetic equator. The solutions are then labeled by the fixed rest mass and radiation energy fluxes.

To the steady Euler equation for a cold, relativistic MHD fluid, we add a term representing the radiation force,

$$\rho \Gamma \mathbf{v} \cdot \nabla (\Gamma \mathbf{v}) = \frac{1}{4\pi} [(\nabla \cdot \mathbf{E})\mathbf{E} + (\nabla \times \mathbf{B}) \times \mathbf{B}] + \frac{\Gamma \rho}{\bar{m}} \mathbf{F}^{\text{rad}}. \quad (15)$$

Taking the dot product of equation (15) with the poloidal magnetic field \mathbf{B}_p gives

$$\begin{aligned} \left(B_r \partial_r + \frac{B_\theta}{r} \partial_\theta \right) \Gamma c^2 - \frac{v_\phi}{r} \left[B_r \partial_r (r \Gamma v_\phi) + \frac{B_\theta}{\sin \theta} \partial_\theta (\sin \theta \Gamma v_\phi) \right] = \\ - \frac{B_\phi}{4\pi \Gamma \rho r} \left[B_r \partial_r (r B_\phi) + \frac{B_\theta}{\sin \theta} \partial_\theta (\sin \theta B_\phi) \right] + \frac{1}{\bar{m}} (B_r F_r^{\text{rad}} + B_\theta F_\theta^{\text{rad}}). \end{aligned} \quad (16)$$

The projection of the Coulomb force onto \mathbf{B}_p vanishes in a steady, axisymmetric MHD outflow with $E_\phi = 0$, since then $\mathbf{E} \cdot \mathbf{B} = \mathbf{E}_p \cdot \mathbf{B}_p = 0$. The ϕ -component of equation (15) is

$$\frac{v_r}{r} \partial_r (r \Gamma v_\phi) + \frac{v_\theta}{r \sin \theta} \partial_\theta (\Gamma v_\phi \sin \theta) = \frac{1}{4\pi \Gamma \rho r} \left[B_r \partial_r (r B_\phi) + \frac{B_\theta}{\sin \theta} \partial_\theta (\sin \theta B_\phi) \right] + \frac{1}{\bar{m}} F_\phi^{\text{rad}}. \quad (17)$$

The toroidal and poloidal components of \mathbf{B} are related through the flux-freezing condition (8).

The photon emission radius r_s serves as a reference length, and the photon compactness is also measured at this radius:

$$x \equiv \frac{r}{r_s}; \quad \omega \equiv \frac{\Omega_f r_s}{c}; \quad \chi_s \equiv \frac{\sigma_T L_\gamma}{4\pi r_s \bar{m} c^3}. \quad (18)$$

In a GRB outflow, the photosphere generally lies outside the light cylinder of the rotating engine, so we take $\omega = \Omega_f r_s / c > 1$ in our calculations. For example, an outflow launched by a millisecond engine which fills an opening angle $\theta \sim 0.1$ at a breakout radius of $\sim 10^{10}$ cm will have a physical width $\Omega_f r \sin \theta / c \sim 100$ times larger than the engine light cylinder.² This means that only a tiny fraction $\sim 10^{-5} - 10^{-3}$ of the solid angle of a laminar jet will rotate rapidly enough that our approximation breaks down. (In practice, a modest amount of turbulence in the jet could mix this thin inner cone with the much wider, slowly rotating annulus surrounding it.) In practice, for computational ease, we consider intermediate values of ω . In the case of an isolated millisecond magnetar one might indeed have $\omega \sim 1$.

The magnetization is defined by

$$\sigma \equiv \frac{B_r^2 \Omega_f^2 r^2 \sin^2 \theta}{4\pi \Gamma \rho v_r c^3} \quad (19)$$

which is constant in the monopolar outflow considered here.³ The kinetic, Poynting and radiation luminosities, $\Gamma \dot{M} c^2$, L_P and L_γ , are related by

$$\frac{L_P}{\Gamma \dot{M} c^2} = - \frac{\sigma}{\Gamma x \omega \sin \theta} \frac{B_\phi}{B_r} \sim \frac{\sigma}{\Gamma}; \quad \frac{L_\gamma}{\Gamma \dot{M} c^2} \sim \frac{1}{6\Gamma^2(x_\tau)x_\tau} \frac{\chi_s}{\Gamma}, \quad (20)$$

where in the last equality we have assumed that the flow is relativistic [see equation (3)]. When radiation is absent, the energy and angular momentum per unit rest mass,

$$\mu = \Gamma - \frac{\sigma}{x \omega \sin \theta} \frac{B_\phi}{B_r}; \quad \mathcal{L} = \Gamma x \sin \theta \beta_\phi - \frac{B_\phi \sigma}{B_r \omega^2 x \sin \theta} \quad (21)$$

are conserved along field lines.

3.1. Relativistic Radiation Force

The radiation emanates from a spherical static ‘emission surface’ of radius r_s ($x = 1$). We adopt simplified spectral and angular distributions: the unscattered radiation is monochromatic, uniform at angles $0 < \theta < \pi/2$ at the emission surface, and streams freely outward. At $x > 1$, the cone of the radiation field contracts and

$$I_\nu = I_0 \nu_0 \delta(\nu - \nu_0) \quad \text{for} \quad \theta < \theta_s \equiv \sin^{-1} \left(\frac{r_s}{r} \right) = \sin^{-1} \left(\frac{1}{x} \right); \quad I_\nu = 0 \quad \text{for} \quad \theta > \theta_s. \quad (22)$$

This accurately represents an isotropically emitting star that is surrounded by an optically thin wind. It still produces qualitatively correct results if the outflow is optically thick near the engine, and experiences nearly linear growth of Lorentz factor with radius, driven by radiation pressure (Section 3.2).

² Early claims of measurements of jet opening angles based on temporal breaks in GRB afterglow light curve (e.g. Rhoads 1999) have been revealed to be somewhat ambiguous based on more complicated behavior seen in the Swift data (e.g. Zhang et al. 2006). Nonetheless in a few cases detailed fits with direct hydrodynamical modelling are consistent with opening angles ~ 0.1 (e.g. van Eerten et al. 2012), and a range of a few around this value seems likely (e.g. Panaitescu & Kumar 2002).

³ This definition, following Michel (1969) and Goldreich & Julian (1970), differs in terms $O(v_\phi / \Omega_f r \sin \theta_f)$ to both $\sigma = (c^2 d\dot{M} / d\Omega)^{-1} dL_P / d\Omega$, and $\sigma = (c^3 d\dot{M} / d\Omega)^{-1} \dot{\Phi}_\phi^2$, where $\dot{\Phi}_\phi = v_r r \sin \theta_f B_\phi$ is the advection rate of toroidal flux. With this definition σ is independent of radius if the poloidal field is restricted to be purely radial, but the last two definitions are non-constant at $O(v_\phi / \Omega_f r \sin \theta_f)$.

Because $\omega \gg 1$ typically, a non-rotating emission surface is a reasonable approximation. The effect of adding modest rotation to the photon source is addressed quantitatively in Appendix A, and the corrections to the flow solution are shown to be small.

The radiation interacts with electrons (and positrons) via Thomson scattering, and the radiative force is taken to be unperturbed by this interaction. The radiation force per scattering charge in a global inertial ('lab') frame is related to the force $\mathbf{F}^{\text{rad}'}$ in the flow rest frame by

$$\mathbf{F}^{\text{rad}} = \left[\mathbf{F}^{\text{rad}'} - (\mathbf{F}^{\text{rad}'} \cdot \boldsymbol{\beta}) \frac{\boldsymbol{\beta}}{\beta^2} \right] \Gamma^{-1} + (\mathbf{F}^{\text{rad}'} \cdot \boldsymbol{\beta}) \frac{\boldsymbol{\beta}}{\beta^2}, \quad (23)$$

where primes denote quantities in the frame co-moving with the fluid. Letting $\hat{\mathbf{k}}$ be the unit wave vector of the incoming photon, we have the transformations

$$\begin{aligned} I'_\nu &= I_\nu \Gamma^3 (1 - \boldsymbol{\beta} \cdot \hat{\mathbf{k}})^3; & dv' &= dv \Gamma (1 - \boldsymbol{\beta} \cdot \hat{\mathbf{k}}); & d\Omega' &= \frac{d\Omega}{\Gamma^2 (1 - \boldsymbol{\beta} \cdot \hat{\mathbf{k}})^2}; \\ \hat{\mathbf{k}}' &= \frac{\hat{\mathbf{k}} + (\Gamma - 1)(\hat{\boldsymbol{\beta}} \cdot \hat{\mathbf{k}})\hat{\boldsymbol{\beta}} - \boldsymbol{\beta}\Gamma}{\Gamma(1 - \boldsymbol{\beta} \cdot \hat{\mathbf{k}})}. \end{aligned} \quad (24)$$

The radiation force in the fluid frame is given by

$$\mathbf{F}^{\text{rad}'} \equiv \frac{d\mathbf{p}'}{dt'} = \frac{\sigma_T}{c} \int I'_\nu \hat{\mathbf{k}}' d\Omega' dv' = \frac{\sigma_T I_0 \nu_0}{c} \int \Gamma^2 (1 - \boldsymbol{\beta} \cdot \hat{\mathbf{k}}) \left[\hat{\mathbf{k}} \Gamma^{-1} + (1 - \Gamma^{-1}) \left(\frac{\boldsymbol{\beta} \cdot \hat{\mathbf{k}}}{\beta^2} \right) \boldsymbol{\beta} - \boldsymbol{\beta} \right] d\Omega, \quad (25)$$

and combining with equation (23) gives

$$\mathbf{F}^{\text{rad}} = \frac{\sigma_T I_0 \nu_0}{c} \int (1 - \boldsymbol{\beta} \cdot \hat{\mathbf{k}}) \left[\hat{\mathbf{k}} - \boldsymbol{\beta} \Gamma^2 (1 - \boldsymbol{\beta} \cdot \hat{\mathbf{k}}) \right] d\Omega. \quad (26)$$

The radiation force (26) can be evaluated analytically by integrating over the emission surface. Defining dimensionless functions R, P , by

$$F_r^{\text{rad}} = \chi_s \frac{\bar{m}c^2}{r_s} R(r, \Gamma); \quad F_\phi^{\text{rad}} = \chi_s \frac{\bar{m}c^2}{r_s} P(r, \Gamma), \quad (27)$$

one finds

$$R = -\frac{8}{3}u\Gamma + \frac{1+2u^2}{x^2} + \beta_r (2\Gamma^2 + v^2) \sqrt{1 - \frac{1}{x^2}} + \beta_r \left(\frac{2}{3}\Gamma^2 - v^2 \right) \left(1 - \frac{1}{x^2} \right)^{3/2}; \quad (28)$$

$$P = -\beta_\phi \left[\frac{8}{3}\Gamma^2 - \frac{2u\Gamma}{x^2} - (1 + 2\Gamma^2 + v^2) \sqrt{1 - \frac{1}{x^2}} + \frac{1}{3} (1 - 2u^2 + v^2) \left(1 - \frac{1}{x^2} \right)^{3/2} \right], \quad (29)$$

where the radial and non-radial four-velocities are

$$(\mathbf{u}, \mathbf{v}) \equiv (\Gamma\beta_r, \Gamma\beta_\phi). \quad (30)$$

At large radius and Lorentz factor, expressions (28) and (29) simplify to

$$R \simeq \frac{1}{4x^2\Gamma^2} - \frac{\Gamma^2}{12x^6}; \quad P \simeq -\frac{\beta_\phi}{2x^2} \left(\frac{1}{2\Gamma^2} + \frac{1}{x^2} + \frac{\Gamma^2}{6x^4} \right). \quad (31)$$

The first term in the radial force is due to photons propagating nearly parallel to the fluid; the second is the drag caused by photons which are aberrated into the anti-radial direction by the relativistic particle motion. The photon field seen by the particle is nearly isotropic in a frame where $R = 0$. At large χ_s and x not too large, the matter therefore tends toward the equilibrium Lorentz factor

$$\Gamma_{\text{eq}} \simeq 3^{1/4} \left(\frac{r}{r_s} \right) = 3^{1/4} x. \quad (32)$$

This frame only exist due to the extended nature of the source.

3.2. Photon Distribution at a Displaced Photosphere

In many cases, the outflow moves relativistically at its scattering photosphere, so that the radiation field is already collimated at the base of the transparent zone. Then the emission surface becomes a virtual one. Setting the photospheric Lorentz factor to the equilibrium value (32), the emission surface is pushed inward to a radius

$$r_{s,\text{eff}} = 3^{1/4} \frac{r_\tau}{\Gamma(r_\tau)}. \quad (33)$$

A radiation field that emerges from a relativistically moving photosphere is not cut off sharply at an angle $\theta_s = r_{s,\text{eff}}/r_\tau = 3^{1/4}/\Gamma(r_\tau)$, but has a somewhat smoother cutoff. Consider, instead, an intensity that is isotropic in the matter rest frame, $I'_\nu =$

$I_0^R \nu_0^R \delta(\nu' - \nu_0^R)$, and compare with the top-hat spectral distribution (22) by normalizing to a fixed flux in the frame of the engine, $F = 2\pi \int d\mu \int d\nu I_\nu(\mu)$. Then the frequency-integrated intensity in the lab frame is

$$I(\theta) = \int d\nu I_\nu(\theta) = \frac{I_0^R \nu_0^R}{[\Gamma(1-\beta\mu)]^4} \simeq \frac{I(\theta=0)}{(1+\Gamma^2\theta^2)^4} = \frac{3^{3/2}}{(1+\sqrt{3}\theta^2/\theta_s^2)^4} \frac{F}{\pi\theta_s^2} \quad \left(\Gamma = \Gamma_{\text{eq}} = \frac{3^{1/4}}{\theta_s} \right), \quad (34)$$

as compared with $I = F/\pi\theta_s^2$ for $\theta < \theta_s$.

These two angular distributions yield the same photon force for a static charge at $r \gg r_{s,\text{eff}}$ and, by construction, the same Lorentz factor for which the radiation force vanishes. The power with which an electron scatters photons in the bulk frame is nearly identical as well: $P' = 4\pi \int d\nu' \sigma_T I_{\nu'} = 3\sigma_T F/4\Gamma^2$ for the isotropic bulk-frame intensity, and

$$P' = \left(1 + \sqrt{3} \frac{\Gamma^2}{\Gamma_{\text{eq}}^2} + \frac{\Gamma^4}{\Gamma_{\text{eq}}^4} \right) \frac{\sigma_T F}{4\Gamma^2} = \left(\frac{1}{2} + \frac{\sqrt{3}}{4} \right) \frac{\sigma_T F}{\Gamma_{\text{eq}}^2} \quad (\Gamma = \Gamma_{\text{eq}}) \quad (35)$$

for the top-hat distribution. The spectrum of photons scattered by a cold electron flow is proportional to P' , and differs in normalization by $\sim 20\%$ in the two cases.

More generally, if the outflow interacts with slower relativistic material – as discussed by Thompson (2006) in the context of GRBs – then the beam of photospheric photons is scattered into a cone of width $> 1/\Gamma$. This motivates our considering outflows with i) significant scattering optical depth at $r = r_s$; but ii) $\Gamma(r_s) > 1$. Given the potential importance of such additional effects for GRBs, we stick with the simplest model a photon emission surface with uniform intensity, with the understanding that this a virtual surface in some circumstances. See Section 6 for calculations of the scattered photon spectrum and the application to GRBs.

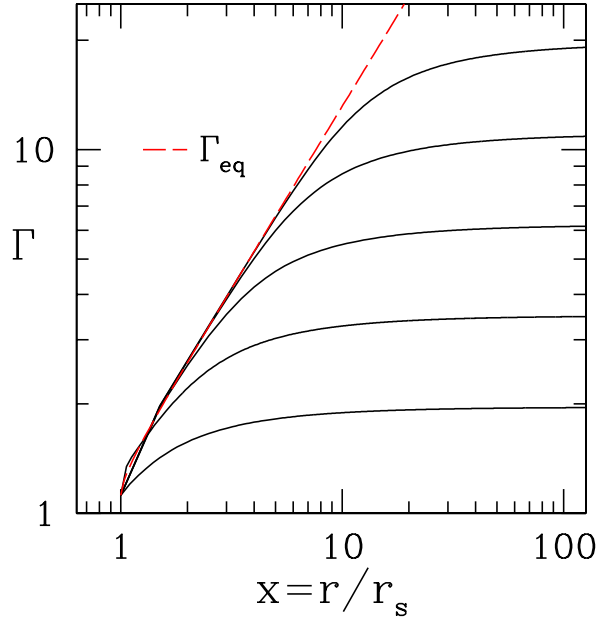


FIG. 1.— Radiative acceleration of an unmagnetized outflow by a photon source at $x = 1$. The compactness χ_s is varied from 10^{-10} to 10^5 . Here $\Gamma_{\text{eq}} = 3^{1/4}x$.

3.3. Acceleration of an Unmagnetized Outflow

As a test of our formalism, we revisit the acceleration of cold matter by an intense radiation field, setting $\sigma = 0$. Then equations (15), (27) and (28) combine to give

$$\frac{d\Gamma}{dx} = \chi_s \left(R + \frac{v}{u} P \right); \quad \frac{d\beta_\phi}{dx} = -\frac{\beta_\phi}{x} - \chi_s \left[\frac{\beta_\phi}{\Gamma} R - \frac{(1-\beta_\phi^2)}{u} P \right], \quad (36)$$

and simplify further to

$$\frac{d\Gamma}{dx} \simeq \chi_s R \simeq \frac{\chi_s}{4x^2} \left(\frac{1}{\Gamma^2} - \frac{\Gamma^2}{3x^4} \right); \quad \frac{d\beta_\phi}{dx} \simeq -\frac{\beta_\phi}{x} - \frac{\chi_s \beta_\phi}{2x^2 \Gamma} \left(\frac{1}{\Gamma^2} + \frac{1}{x^2} \right) \quad (37)$$

for large x , Γ . The matter Lorentz factor tracks Γ_{eq} until the local compactness $\chi \sim \chi_s/\Gamma^3 x$ drops below $\sim \Gamma$ (see Figure 1). The asymptotic Lorentz factor is

$$\Gamma_\infty \simeq 1.086\chi_s^{1/4} \quad (38)$$

as long as baryon loading is sufficiently low ($\eta \equiv L_\gamma/\dot{M}c^2 \gg \chi_s^{1/4}$); otherwise $\Gamma_\infty \simeq \eta$.

The radiation force has a stronger effect when the flow remains optically thick out to a large distance from the engine, and develops at least a moderate Lorentz factor before the photons begin to stream freely.

In this situation, the constraint $L_\gamma < L_p$ would correspond to a limit on the photon compactness as measured at the photosphere,

$$\chi(r_\tau) \equiv \frac{L_\gamma \sigma_T}{4\pi r_\tau m_e c^3} = \frac{r_s}{r_\tau} \chi_s, \quad (39)$$

namely,

$$\chi(r_\tau) \lesssim 6\Gamma^2(r_\tau)\sigma \quad (40)$$

[see equation (20)]. Now the parameter χ_s describes a ‘virtual’ photon source that is buried at large scattering depth, and is already collimated at the photosphere. The terminal Lorentz factor increases to

$$\Gamma_{\infty,\chi} \sim \chi_s^{1/4} = \left[3^{-1/4}\Gamma(r_\tau)\chi(r_\tau)\right]^{1/4}. \quad (41)$$

If the fast point were to sit in the transparent zone, then $\Gamma(r_\tau) \lesssim \sigma^{1/3}$ and one has the bound

$$\chi_\tau \lesssim 6\sigma^{5/3}; \quad \Gamma_{\infty,\chi} \lesssim 1.3\sigma^{1/2}. \quad (42)$$

If the bound (42) is not satisfied, then the outflow will pass through the fast critical point before reaching its photosphere. Nonetheless, the radiation field will provide significant supplemental acceleration outside the photosphere for any value of $\Gamma(r_\tau)$ below σ .

4. DIMENSIONLESS OUTFLOW EQUATIONS: $\theta \lesssim \pi/2$

The poloidal magnetic field lines make a transition from dipolar to nearly radial at the light cylinder of an isolated pulsar, being forced open by causality constraints (Contopoulos 2005; McKinney 2006; Spitkovsky 2006). More collimated outflows are expected from magnetized stars surrounded by accretion disks (Blandford & Znajek 1977; Blandford & Payne 1982), and are the focus of paper II.

We consider a streamline close to the magnetic equator (but not so close as to involve the equatorial current sheet). We work with a simplified form of the Euler equations that includes the radiation force, but assumes the poloidal magnetic field to be purely radial. Therefore we substitute

$$B_r \simeq \frac{B_{r,s}}{x^2}; \quad \frac{B_\theta}{B_r} = \frac{v_\theta}{v_r} \ll 1; \quad \sin\theta \simeq 1, \quad (43)$$

into equations (16), (17), which gives

$$\partial_r \Gamma c^2 - \frac{v_\phi}{r} \partial_r (r\Gamma v_\phi) = -\frac{B_\phi}{4\pi\Gamma\rho r} \partial_r (rB_\phi) + \frac{1}{m} F_r^{\text{rad}}; \quad (44)$$

$$\frac{v_r}{r} \partial_r (r\Gamma v_\phi) = \frac{B_r}{4\pi\Gamma\rho r} \partial_r (rB_\phi) + \frac{1}{m} F_\phi^{\text{rad}}. \quad (45)$$

The various terms in the right-hand sides of these equations can be separated into purely magnetocentrifugal pieces (which do not depend on the radiation force), the direct radiation force, and a cross term:

$$\frac{d\Gamma}{dx} = \frac{\Gamma'_\sigma + \Gamma'_\chi + \Gamma'_{\sigma\chi}}{\mu_{\text{eff}}}; \quad \frac{d\beta_\phi}{dx} = \frac{\beta'_{\phi,\sigma} + \beta'_{\phi,\chi} + \beta'_{\phi,\sigma\chi}}{\mu_{\text{eff}}}, \quad (46)$$

where

$$\Gamma'_\sigma + \Gamma'_\chi + \Gamma'_{\sigma\chi} \equiv -\frac{\sigma}{\beta_r x \omega} \left[\frac{\beta_\phi}{x} \left(2 + \frac{\beta_\phi B_\phi}{\beta_r B_r} \right) \right] + \chi_s \left(R + \frac{\beta_\phi P}{\beta_r} \right) - \frac{\sigma \chi_s}{u x^2 \omega^2} \left(1 + \frac{\beta_\phi B_\phi}{\beta_r B_r} \right) \left(R + \frac{B_\phi P}{B_r} \right); \quad (47)$$

$$\begin{aligned} \beta'_{\phi,\sigma} + \beta'_{\phi,\chi} + \beta'_{\phi,\sigma\chi} &\equiv -\frac{\beta_\phi}{x} \left[1 + \frac{\sigma}{u x^2 \omega^2} - \frac{\sigma}{u^3} - \frac{\beta_\phi \sigma}{u x \omega} \left(1 - \frac{1}{u^2} \right) \right] \\ &\quad - \chi_s \left[\frac{\beta_\phi}{\Gamma} R - \frac{(1-\beta_\phi^2)}{u} P \right] - \frac{\sigma \chi_s}{x^2 \omega^2 \Gamma^2 u^2} \frac{B_\phi}{B_r} \left(R + \frac{B_\phi P}{B_r} \right), \end{aligned} \quad (48)$$

and

$$\mu_{\text{eff}} = 1 - \frac{\sigma}{u^3} (1 + v^2) - \frac{\sigma}{u x^2 \omega^2} \left(1 + \frac{v^2}{u^2} \right) + \frac{2\sigma v \Gamma}{u^3 x \omega}. \quad (49)$$

4.1. Flow Through the Fast Critical Point: $\theta \lesssim \pi/2$, $B_r \sim r^{-2}$

These MHD wind equations have critical points where the flow matches the speed of a cold MHD mode. The Alfvén critical point corresponds to a flow speed $u = \sigma(1 - \omega^2 x^2)/\omega^2 x^2$, and therefore sits inside the light cylinder.

Since we are looking for robust flow solutions which do not depend on the magnetic field structure in this inner zone (Section 2.2), our focus is on the fast critical point, where

$$u = \frac{\sigma}{x^2 \omega^2} \left(1 - \omega^2 x^2 + \frac{B_\phi^2}{B_r^2} \right). \quad (50)$$

This is the singularity appearing in equation (46). A regular flow solution passing through this point must satisfy two conditions:

$$\Gamma'_\sigma(x_c) + \Gamma'_\chi(x_c) + \Gamma'_{\sigma\chi}(x_c) = 0; \quad \mu_{\text{eff}}(x_c) = 0. \quad (51)$$

Here x_c is the (so-far undetermined) radius of the fast point. Equations (51) generate a one parameter family of flow solutions.

The specific angular momentum evolves according to the simple equation $d\mathcal{L}/dx = (x/\beta_r)\chi_s P$. We have tested equations (44) and (45) by combining them and re-deriving this equation. This means that the critical point of the equation for $d\beta_\phi/dx$ does not impose independent constraints on the flow solution: a solution with a smooth $\Gamma(x)$ profile automatically satisfies the $\beta'_{\phi,\sigma}(x_c) + \beta'_{\phi,\chi}(x_c) + \beta'_{\phi,\sigma\chi}(x_c) = 0$.

The presence of a cross term in the wind equations, involving both the magnetization σ and the compactness χ_s , deserves some comment. Inside the fast magnetosonic point, and outside the Alfvén point, the *radial* motion of the fluid has effectively a negative inertia: a positive external radial force extracts energy from the outflow. This negative inertia arises from the response of B_ϕ , which dominates the energy integral (21), to changes in the radial flow speed. The scaling $B_\phi \sim \beta_r^{-1}$ implies a decrease in toroidal field energy with increasing β_r . On the other hand, the angular momentum (21) is also dominated by the electromagnetic field. A change in B_ϕ creates unbalanced toroidal stresses, which are a source for β_ϕ , and are proportional to $\sigma\chi_s$. Changes in β_ϕ and β_r of opposing signs allow B_ϕ to remain nearly constant. The net change in Lorentz factor is positive, $\delta\Gamma = \Gamma^{-3}(\beta_r\delta\beta_r + \beta_\phi\delta\beta_\phi) > 0$, if $1 + \beta_\phi B_\phi/\beta_r B_r > 0$. Close to the light cylinder, where the term $\sim -\sigma/ux^2\omega^2$ in μ_{eff} dominates the term $-\sigma/u^3$, the effective inertia has the usual sign.

4.2. Pure MHD Wind ($\chi_s = 0$) with Monopolar Radial Magnetic Field

When radiation fields are absent and $\Gamma \gg 1$ our equations reduce to the cold limit of the system studied by Goldreich & Julian (1970). The angular momentum \mathcal{L} [equation (21)] is conserved, and determines

$$\beta_\phi = \frac{x\omega(\mathcal{L}\beta_r - \sigma)}{x^2\omega^2 u - \sigma}. \quad (52)$$

The fast point lies at infinite radius, the Lorentz factor being limited to its critical value

$$\Gamma_{\infty,\sigma} = \sqrt{1 + \sigma^2/3} \simeq \sigma^{1/3}. \quad (53)$$

The unique solution passing through the Alfvén and fast critical points is the minimum-energy solution found by Michel (1969). The slow acceleration of radial flows is an artifact of the near perfect cancellation of the outward magnetic pressure gradient force and the inward curvature force. Faster acceleration is possible through a faster-than-spherical divergence of the outflow (Begelman & Li 1994), or differential bending of the poloidal field lines (Tchekhovskoy et al. 2009), the effect of which we examine in paper II.

4.3. Small Compactness Limit: $\chi_s \ll 4\sigma^{4/3}\omega^{-2}$

For small but finite χ_s , the Lorentz factor at the fast point remains unchanged from the pure MHD solution, $\Gamma_c \simeq \sigma^{1/3}$, but the critical point is brought in to a finite radius. The pure magnetocentrifugal and radiation terms in the wind equations dominate at large x, Γ , and simplify to

$$\Gamma'_\sigma \simeq -\frac{v\sigma}{ux^2\omega} \left(2 - \frac{\beta_\phi x\omega}{\beta_r^2} \right) \simeq -\frac{v\sigma}{ux^2\omega}; \quad \Gamma'_\chi \simeq \chi_s R \simeq \frac{\chi_s}{4x^2\Gamma^2} \quad (54)$$

Applying the regularity condition $\Gamma'_\sigma + \Gamma'_\chi \simeq 0$ at the critical point gives

$$x_c \simeq \frac{4\sigma^{5/3}}{\chi_s\omega^2}; \quad \beta_{\phi,c} \simeq \frac{1}{x_c\omega} \simeq \frac{\chi_s\omega}{4\sigma^{5/3}}; \quad \mathcal{L}_c \simeq \Gamma_c x_c \beta_{\phi,c} + \frac{\sigma}{\omega\beta_{r,c}} \simeq \frac{\sigma^{1/3}}{\omega} (1 + \sigma^{2/3}) \quad (\text{low } \chi_s). \quad (55)$$

4.4. Large Compactness Limit: $\chi_s \gg 4\sigma^{4/3}\omega^{-2}$

For very large χ_s the fluid is locked to the radiation field while crossing the fast point at a finite radius,

$$\Gamma_c \simeq \Gamma_{\text{eq}} \Rightarrow x_c \simeq 3^{-1/4}\Gamma_c \quad (\text{high } \chi_s). \quad (56)$$

Here B_r need not be small compared with B_ϕ . Approximating $\beta_\phi \ll x\omega$ and making use of equation (8), equation (50) becomes

$$u^3 \simeq \sigma \left(1 + \Gamma^2 \frac{B_r^2}{B_\phi^2} \right) \simeq \frac{B_\phi^2 + \Gamma^2 B_r^2}{4\pi u \rho c^2} \quad (57)$$

Substituting $u_c \simeq \Gamma_c \simeq 3^{1/4} x_c$ gives the critical point parameters

$$\Gamma_c \simeq \sigma^{1/3} \left(1 + \frac{\sqrt{3}}{\omega^2}\right)^{1/3} \quad \mathcal{L}_c \simeq \frac{\sigma}{\omega} \left(1 + \frac{1}{2}\Gamma_c^{-2}\right) \quad (\text{high } \chi_s). \quad (58)$$

The transition between the low- and high- χ_s scalings for the fast point occurs where $x_{c,\text{low}} \simeq x_{c,\text{high}}$, at a compactness $\chi_s \simeq 4\sigma^{4/3}\omega^{-2}$.

4.5. Numerical Methods and Boundary Values

The singularity at the fast point is difficult to handle with standard integration methods, especially when the wind equations become stiff, as they do when $\chi_s \gg 1$. We employ two different integration schemes: a shooting method for low χ_s , and a relaxation method for high χ_s . The position x_c of the critical point is unknown *a priori*, since the regularity condition provides only one constraint on the two coupled ODEs. Once a candidate value of x_c is chosen, the flow variables at the critical point are uniquely determined, as is the flow solution interior to it. However, this interior solution generally diverges at small radius. A strong divergence is avoided only for a narrow range of x_c , and even then the solution tends to develop sharp gradients in Γ and β_ϕ . Avoiding such gradients leads to an essentially unique choice of x_c and a robust flow solution. We have found that these smooth solutions have the property that the terms in $d\beta_\phi/dx$ which depend explicitly on the radiation field should sum to zero at $x = 1$,

$$(\beta'_{\phi,\chi} + \beta'_{\phi,\sigma\chi})_{x=1} = 0. \quad (59)$$

This recovers Michel's minimum-energy solution (Michel 1969) in the limit of vanishing radiation field, $\chi_s \rightarrow 0$. The resulting initial values of Γ and β_ϕ are plotted in Figure 2 for $\sigma = 10^3$ and $\omega = 2$.

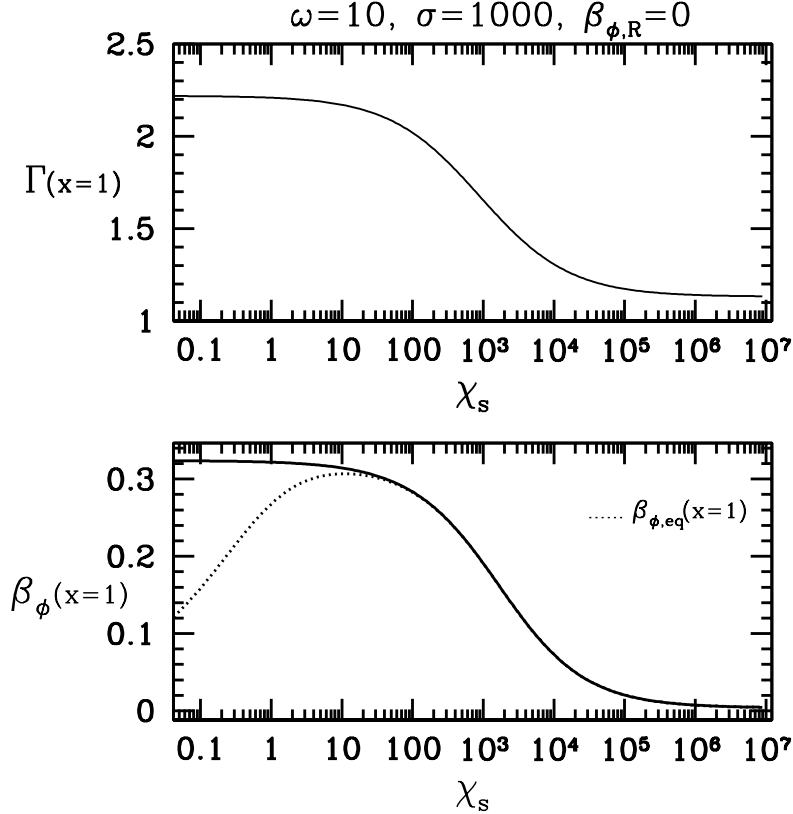


FIG. 2.— Lorentz factor and rotation speed at the inner boundary of an outflow with $\sigma = 10^3$, $\omega \equiv \Omega_f r_s / c = 2$. Dotted line corresponds to a vanishing net toroidal acceleration from the radiation field at the inner boundary, equation (59).

At low χ_s , the flow solution interior to x_c is obtained by first determining the locus of critical points, and the corresponding values of $\Gamma(x_c)$, $\beta_\phi(x_c)$. We then shoot inward from $x = x_c$ using a 5th-order Runge-Kutta algorithm with adaptive step size (see Sections 7.3, 7.5 of Kiusalaas 2010). The value of \mathcal{L}_c – which, unlike x_c , is single valued – is iterated until the required small- x behavior is obtained. This method fails when $\chi_s \gtrsim 100$, since the equations become extremely stiff near $x = 1$, and machine precision becomes inadequate to distinguish values of $\{x_c, \Gamma(x_c), \beta_\phi(x_c)\}$ that lead to converging and diverging solutions.

At high χ_s , we use the relaxation method described in London & Flannery (1982) for transonic hydrodynamic flows. The wind equations are replaced by finite-difference equations on a grid. Starting with a simple trial solution, and an initial guess for x_c ,

the inner boundary condition (59) is applied along with the regularity condition (51) at the critical point. Since the location of the critical point is unknown, an independent variable q which labels mesh points is introduced, along with a mesh-spacing function $Q(x) = \Psi q$ (where Ψ is an unknown number). We choose $Q(x) \propto \ln x$, which tightly packs the grid points near $x = 1$ (where the equations are stiff), and spreads them out near the critical point (so as to avoid divergences induced by the singularity). This necessitates adding two more ODEs, for $x(q)$ and Ψ . The error in the initial guess at grid point i is quantified in terms of $E_i = y_i - y_{i-1} - (x_i - x_{i-1})dy/dx$ and a new solution is obtained by a multi-dimensional Newton-Raphson method (see section 18.3 of Press et al. 2007). The matrix inversion is performed using a Gaussian pivoting algorithm detailed in Kiusalaas (2010). The critical point must be approached from below with this method and so the trial solution is typically cut off at $\sim 90\%$ of the expected critical radius. This method fails in the low χ_s regime since the critical point is at large radius where $d\Gamma/dx \simeq 0$, and even a slight overshoot in Γ_c will be catastrophic.

In both the low and high χ_s regimes, the solution is completed by shooting outward from the critical point.

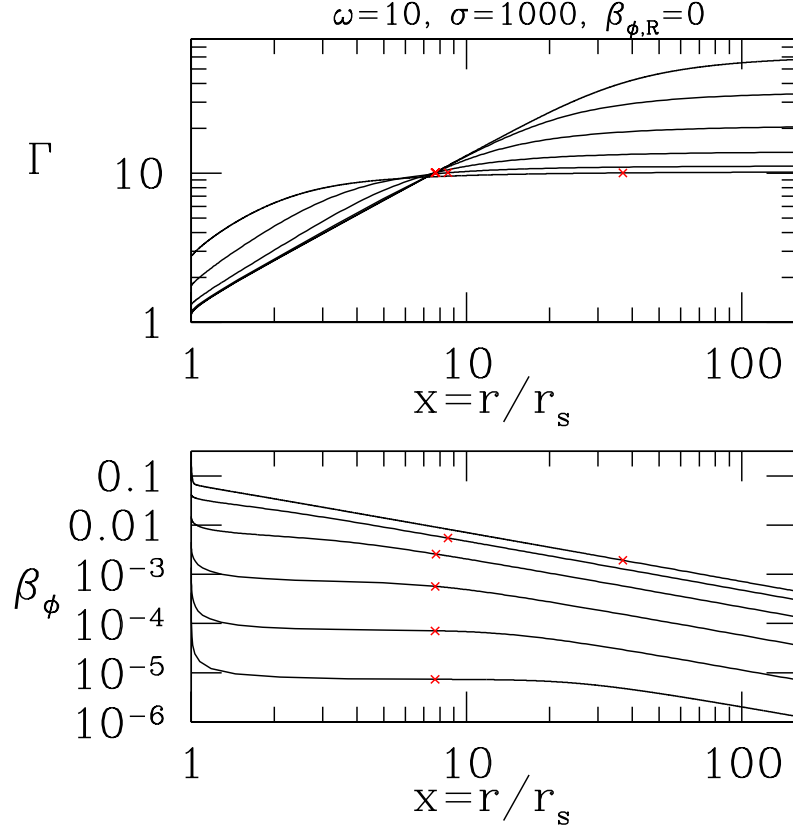


FIG. 3.— Acceleration of a magnetized outflow ($\sigma = 10^3$, $\omega \equiv \Omega_f r_s / c = 10$) for varying compactness of a radiation source situated at $x = 1$: $\chi_s = 10^2 - 10^7$, bottom-top on the right side in $\Gamma(x)$, top-bottom in $\beta_\phi(x)$.

5. RESULTS

As the initial radiation compactness χ_s is increased, the plasma accelerates faster at small radius, and reaches a higher terminal Lorentz factor. The radiation field is weakly collimated near the emission radius, and so the starting Lorentz factor is reduced at large χ_s . Figure 3 shows the dependence of Γ and β_ϕ on radius, obtained for a strongly magnetized outflow ($\sigma = 10^3$), starting from 10 times the light cylinder radius ($\omega = 10$). The Lorentz factor profile shows a smooth transition from Michel's minimum-energy solution in the low- χ_s limit, to the purely radiation-driven solution at large χ_s . An explicit comparison of magnetized and unmagnetized flows is made in Figure 4. Once seen magnetization at a level $\sigma = 10^3$ makes little difference to $\Gamma(x)$ for $\chi_s \gtrsim 10^5$.

The reduction in the starting Lorentz factor by radiation drag is tied to the negative inertia of the plasma inside the fast critical point (Section 4.1). In this inner zone, the inertia is dominated by the magnetic field. A negative radial force, as is provided by the radiation field when $\Gamma > \Gamma_{\text{eq}}$, pushes the flow to higher speeds. The situation reverses at the fast point, where matter begins to dominate the inertia and Γ drops below Γ_{eq} . Outside the fast point, radiation provides a positive push on the matter and the entrained magnetic field. The asymptotic Lorentz factor grows with respect to the cold MHD flow, as we discuss in more detail in Section 5.3.

The fast critical point (marked by the red cross in Figure 3) sits at infinity in the cold MHD wind with monopolar magnetic field, but moves in rapidly as χ_s increases above 10-100. The explicit dependence of the flow properties at the critical point on χ_s is shown in Figure 5 for $\sigma = 10^3$, and two launching radii ($\omega = 10, 2$). Expression (55) provides an excellent fit to the fast critical radius x_c for $\chi_s \lesssim 10^3$, above which it settles to the value where the equilibrium Lorentz factor $\Gamma_{\text{eq}} = \sigma^{1/3}$; see equation (32). The

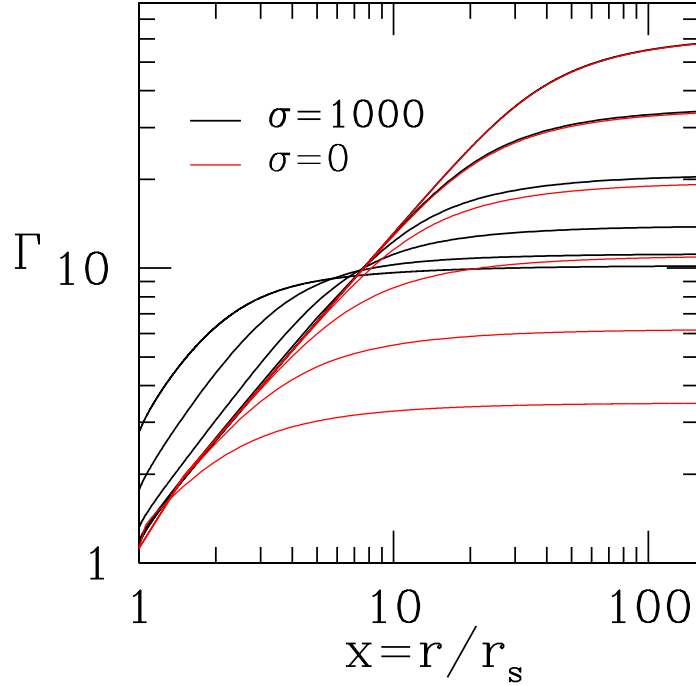


FIG. 4.— Lorentz factor of magnetized (black solid, $\sigma = 10^3$), and unmagnetized (red dotted) outflows, as a function of radius. Compactness of radiation source at $x = 1$ is $\chi_s = 10^2 - 10^7$ (bottom to top on the right side).

radial field inertia causes a small upward adjustment in Γ_c , as may be seen by comparing the cold MHD expression $\Gamma_c \simeq \sigma^{1/3}$ with equation (58). There is a small downward adjustment in the total angular momentum at the critical point.

The coupling of the radiation field to the magnetic field has some subtle effects on the rotation of the outflow. The angular velocity at the critical point decreases with increasing χ_s at large compactness, as would be expected from the increasing friction imparted by radiation field. (The radiation field is assumed not to rotate; the effect of rotation is considered in Appendix A.) However, $\beta_{\phi,c}$ increases with χ_s at small compactness, due to the shrinkage in the critical point radius. The finite value of $\beta_{\phi,c}$ is also worth commenting on. The outward acceleration of the flow requires a finite angular speed for the matter. Strong radiation drag, acting alone, would rapidly damp the matter rotation. However, the radiation field enters indirectly into equation (48) for $d\beta_\phi/dx < 0$ through the term proportional to $\sigma\chi_s$. This cross term represents the reaction of the Lorentz force on the radiation field. It is generally positive and almost exactly cancels the azimuthal radiation drag. (We enforce this condition at $x = 1$, but the condition is nearly satisfied automatically at all radii.) This near cancellation allows the matter to maintain a high enough azimuthal speed to reach the fast critical point. A further interesting effect, evident in Figure 3, involves the near constancy of β_ϕ at small radius in radiation-dominated outflows ($\chi_s \gg \sigma$). This is due to a near cancellation of *all* the terms in $d\beta_\phi/dx$.

5.1. Exchange of Energy Between Radiation and Magnetofluid

In a hot magnetized outflow, the fluid acts to couple the radiation and magnetic field allowing energy to be exchanged between them as the flow accelerates. To study this exchange we write the total energy in terms of kinetic, Poynting and radiation luminosities as

$$\frac{L_K + L_P + L_\gamma}{\dot{M}c^2} = \Gamma - \frac{1}{x\omega \sin\theta} \frac{B_\phi}{B_r} \sigma + \frac{x\chi(x)}{6\tau_{es,s}\Gamma_s^2} \quad (60)$$

where we have taken $\Gamma \propto r$ in calculating the optical depth. For simplicity, our solutions (being calculated in the optically thin regime) assume a constant radiation flux and thus do not strictly conserve energy. Nevertheless, we can impose conservation using the obtained profiles for the kinetic and Poynting fluxes to study the qualitative features of the energy exchange. The results are shown in Figure 6 for various values of photon compactness while taking the optical depth at $r = r_s$ to be unity. The radiation luminosity generally increases sharply at small radius where photons are upscattered by the highly relativistic flow. This must be accompanied by a corresponding decrease in the magnetic energy since the Lorentz force is still accelerating the flow. To see why this occurs note that well outside the light cylinder the Poynting luminosity in a monopolar outflow is $L_P \sim \beta_r^{-1} \sigma \dot{M}c^2$ which can decrease significantly only if the flow is not yet extremely relativistic at the photosphere. In this case field lines are coiled tight and transfer their magnetic energy to the radiation field as they unwind. The matter acts mainly as a catalyst in this process, with relatively small changes in kinetic energy.

Outside the fast point the Poynting flux is essentially constant and further changes in the kinetic energy come directly from the interaction with the photon field. (In Figure 6 the positive/negative slopes of the energy profiles are plotted as dotted/dashed the

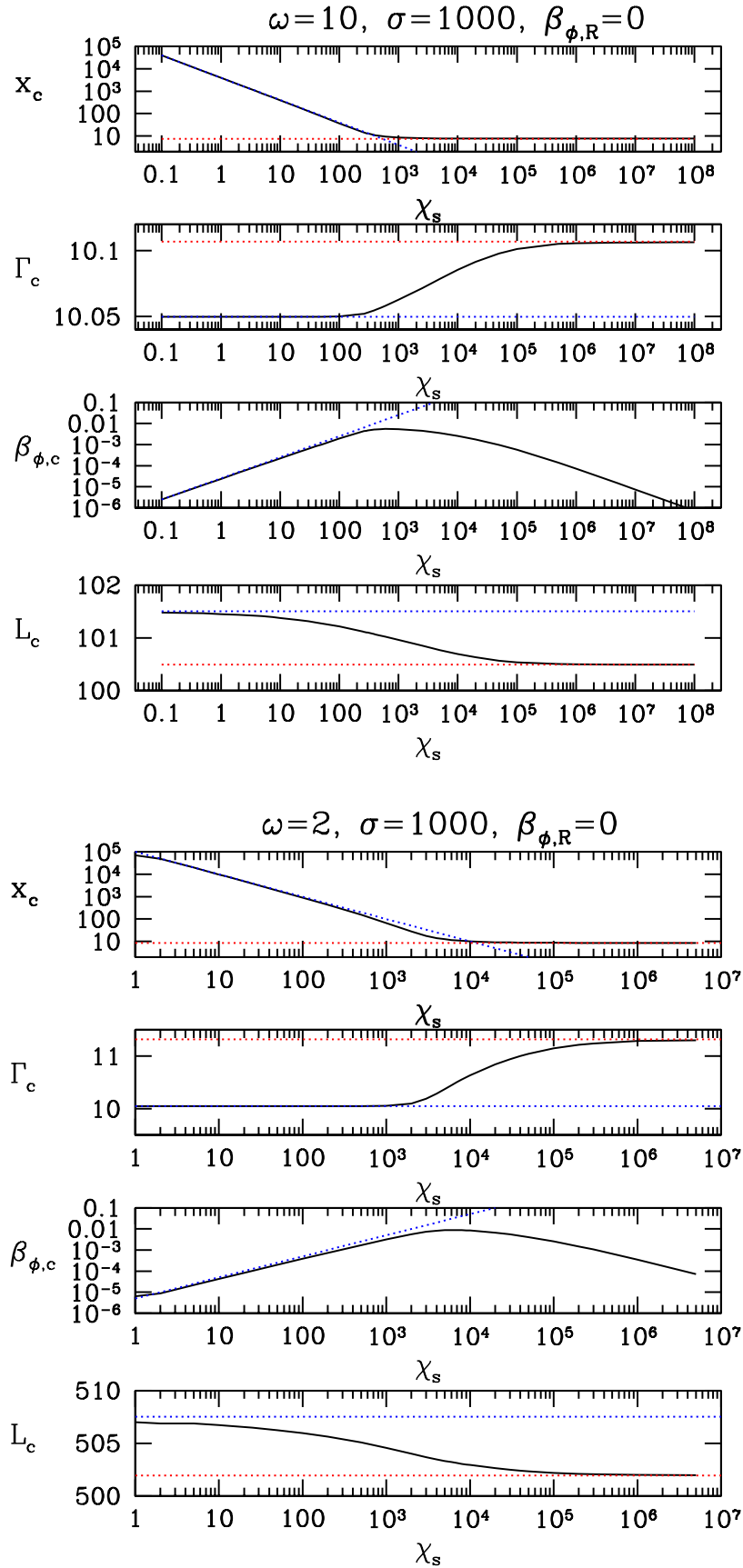


FIG. 5.— *Top panel:* Radius x_c of the fast critical point, and corresponding flow variables Γ , β_ϕ and \mathcal{L} , as a function of radiation compactness χ_s , for $\sigma = 10^3$, $\omega = 10$. Red and blue dotted lines show the analytical approximations (55) (low χ_s) and (58) (high χ_s). *Bottom panel:* Now with a smaller launching radius, $\omega = 2$.

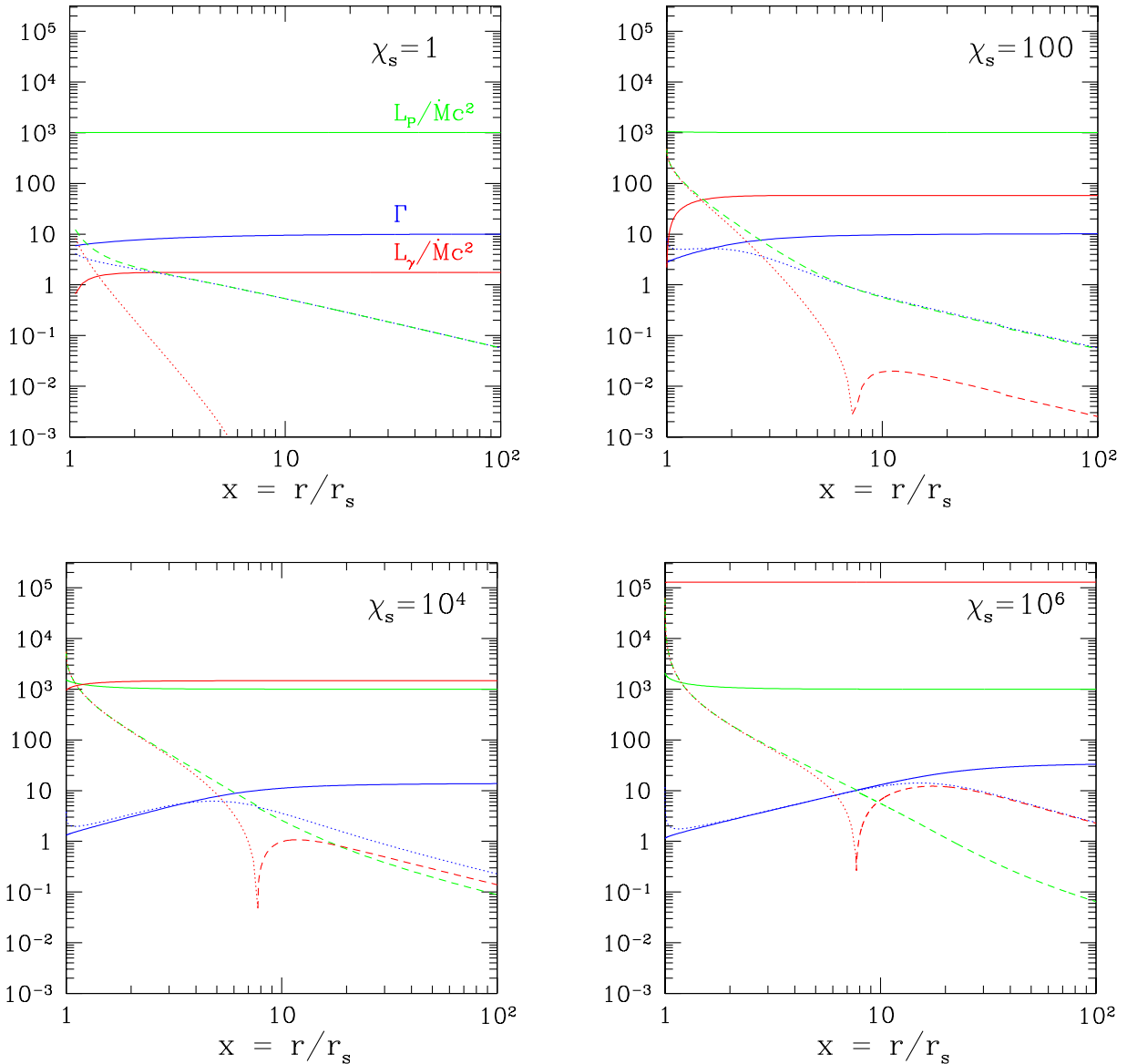


FIG. 6.— Energy exchange in an outflow with $\sigma = 1000$, $\omega = 10$ with an optical depth of unity at $r = r_s$. Poynting, kinetic and radiation luminosities are plotted as solid lines and $dL/d \ln r$ for each is shown in corresponding colors with dotted/dashed representing positive/negative slopes.

corresponding colors.) When χ is high, the fast point marks a sharp transition in the energy exchange: conversion of magnetic to radiation energy inside; conversion of radiation to kinetic energy outside. Accounting for the increase in photon luminosity at small radius would enhance the acceleration outside the fast point.

5.2. Application to Gamma-ray Burst Outflows with Displaced Photospheres

We briefly consider the application of our results to gamma-ray bursts. When a jet emerges from a Wolf-Rayet star, or from a cloud of neutron-rich debris, much of the jet material may experience a strong outward Lorentz force (Tchekhovskoy et al. 2009). Even in that circumstance, the radiation pressure force can enhance or impede the acceleration of the jet material outside its photosphere (Russo & Thompson 2012, Paper II). Other parts of the jet may have unfavorably curved flux surfaces and feel a weaker Lorentz force, more typical of the poloidal field geometry examined in this paper.

Although our solutions are found in the zone exterior to a static, photon-emitting surface, the photon field that emerges from a displaced photosphere will have a similar effect on the outflow exterior to it, if we define an effective source radius $r_{s,\text{eff}}$ as in Section 3.2. A high photon intensity also has the effect of driving the flow profile to a linear relation $\Gamma(r) \propto r$ inside the fast critical point. In that case, the flow profile does not depend on whether the outflow is optically thick or thin inside the critical point. The conditions for this to be the case are outlined at the end of Section 3.3.

To fix some numbers, consider a gamma-ray outflow with an (isotropic) luminosity $4\pi dL_\gamma/d\Omega = 10^{51} L_{51} \text{ erg s}^{-1}$ and a photo-

sphere of radius $r_\tau = 10^{10} r_{\tau,10}$ cm. The corresponding photospheric compactness (1) is $\chi(r_\tau) = 1 \times 10^8 L_{51} r_{\tau,10}^{-1} (m_p/\bar{m})$. Transparency at $r \lesssim r_\tau$ is guaranteed if $\Gamma(r_\tau) \gtrsim 10$, and pairs have mostly annihilated. The effective source radius, obtained by equating the bulk Lorentz factor (32) of the radiation field with $\Gamma(r_\tau)$, is $r_{s,\text{eff}} \sim r_\tau/\Gamma(r_\tau) < 10^9 r_{\tau,10}$ cm. The compactness scaled to this radius, which determines the amplitude of the radiation force in the wind equations (46)-(49), is $\chi_s \gtrsim 10^9 L_{51} r_{\tau,10}^{-1} [\Gamma(r_\tau)/10] (m_p/\bar{m})$.

5.3. Asymptotic Lorentz Factor: Fully Transparent Outflows

Since we are considering a strictly monopolar poloidal magnetic field, the asymptotic Lorentz factor is limited to $\Gamma_{\infty,\sigma} \simeq \sigma^{1/3}$ at small radiation compactness. Higher Lorentz factors are possible at large χ_s , where acceleration is dominated by radiation pressure. First consider the case where the outflow is fully transparent at $r \sim r_s$, and moves transrelativistically near the inner boundary. Then $\Gamma_{\infty,\chi} \simeq 1.086 \chi_s^{1/4}$ (Section 3.3). In the example at the end of the preceding Section, this corresponds to $\Gamma_{\infty,\chi} \sim 200$.

We find a smooth transition between these two limits as shown in Figure 7 for $\sigma = 10^3$ and $\omega = 2, 10$. This is well described by the function

$$\Gamma_\infty^n = \Gamma_{\infty,\sigma}^n + \Gamma_{\infty,\chi}^n, \quad (61)$$

with $n \simeq 2.5$. In this situation, strong radiative acceleration requires a photon source that is not sourced internally by the outflow. Otherwise, the photon luminosity is approximately bounded above by the Poynting luminosity, which implies $L_\gamma \lesssim L_P$ and $\chi_s \lesssim \sigma$.

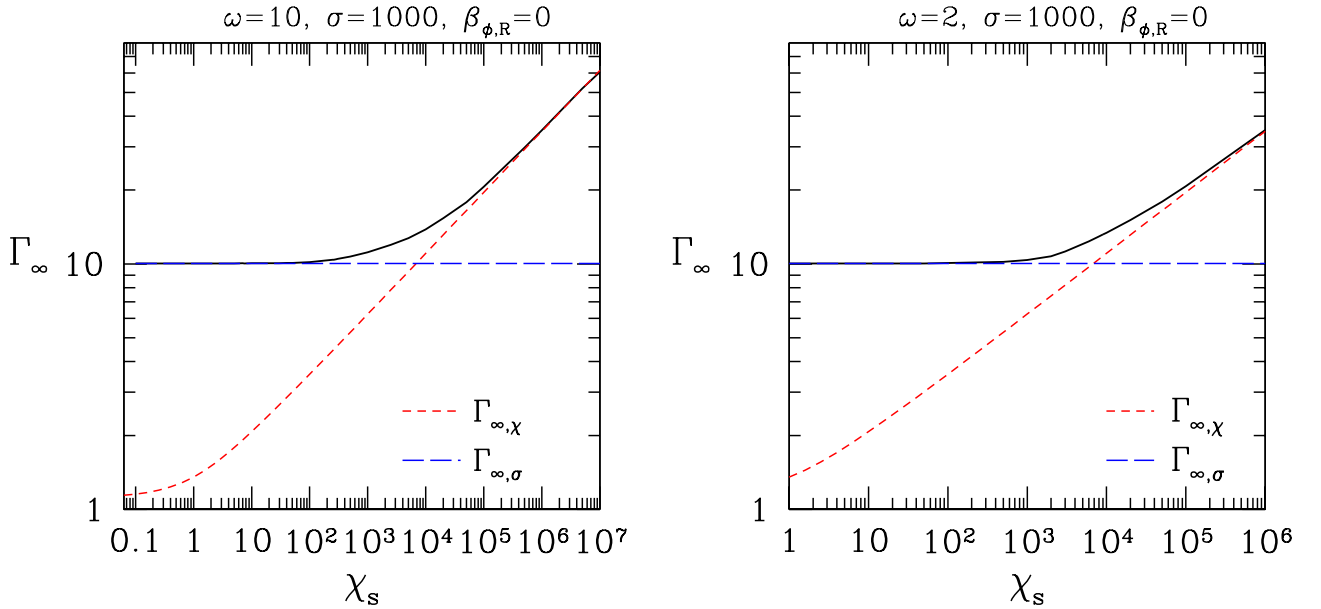


FIG. 7.— Asymptotic Lorentz factor of a magnetized outflow ($\sigma = 10^3$) exposed to a central radiation field with compactness χ_s at $x = 1$. *Left panel:* $\omega = 10$. *Right panel:* $\omega = 2$

6. SPECTRUM OF SCATTERED PHOTONS

The outflowing matter scatters the radiation field, and the frequency distribution of scattered photons is non-thermal. The effect grows stronger as the seed photon beam grows wider with respect to the Lorentz cone, $\theta_s > 1/\Gamma$. We now calculate the spectrum in a situation where most photons see a low optical depth after scattering by the magnetofluid.

To motivate our calculation, it is worth discussing how such a situation could arise in the context of GRBs. Photons which start with a nearly blackbody spectrum will maintain that spectral distribution in a simple relativistic fireball (e.g. Beloborodov 2011; Lazzati et al. 2011). At the photosphere, the photon beam has an opening angle $\theta_s \sim \Gamma^{-1}$ and maintains a nearly isotropic distribution in the bulk frame. So we expect minimal frequency redistribution in MHD outflows that are accelerated mainly by radiation pressure, $\Gamma \sim \Gamma_{\text{eq}}$.

The outflow feels a very strong Lorentz force where neighboring magnetic flux surfaces diverge from each other, and we show in Paper II that this can driven $\Gamma > \Gamma_{\text{eq}}$ even close to the photosphere of a relativistic outflow. But even if this effect is not operating, there is still good reason to expect that material from the progenitor star (in the case of collapsars), or from a preceding neutron-rich wind (in the case of binary NS mergers) will interact with a relativistic MHD outflow. This material can be massive enough to maintain a Lorentz factor Γ_{slow} much lower than that of the MHD outflow, and so broaden the photon beam into a cone of width $\theta_s \sim 1/\Gamma_{\text{slow}}$. For example, a precursor shell, trapped at the head of a relativistic jet, becomes Rayleigh-Taylor unstable

as it is pushed outward, opening out zones of an angular size $\lesssim 1/\Gamma$ in which the jet material can flow freely (Thompson 2006). Another possibility is a jet boundary layer containing material of an intermediate Lorentz factor.

It is, therefore, possible to probe the spectral signature of slow material in a GRB, independent of the details of photon creation at large optical depth. Indeed, because photons moving off the axis of a relativistic flow scatter at a higher rate, this type of interaction can occur even *outside* the photosphere of the MHD outflow, and still result in significant rescattering by the faster material. There are interesting implications for both the high- and low-frequency portions of the photon spectrum.

6.1. Scattering of a Monochromatic Source with Uniform Intensity

We are interested in the power radiated from a steady flow, with a fixed particle density at a given radius. In the case of an impulsive event such as a GRB, of duration Δt , the flow is effectively steady near the transparency surface if $\Gamma^2(r_\tau) \gg r_\tau/c\Delta t$. In this situation, there is no correction between the time coordinate of an observer sitting at a large (but non-cosmological) distance from the engine, and the time coordinate t of the engine rest-frame.

We start with a monochromatic photon source $I_\nu = I_0\nu_0\delta(\nu - \nu_0)$, and the top-hat angular distribution (22) corresponding to a (virtual) emission radius r_s . More general source spectra are then considered by a convolution. The condition of elastic (Thomson) scattering is

$$\tilde{\nu}_{\text{em}} \equiv \frac{\nu_{\text{em}}}{\nu_0} = \frac{1 - \beta\mu}{1 - \beta\mu_{\text{em}}} = \frac{1 + \beta\mu'_{\text{em}}}{1 + \beta\mu'}. \quad (62)$$

The direction cosines of the incident and emitted photons are measured with respect to the radial direction (we neglect any small non-radial motion of the matter), $\mu = \hat{k} \cdot \hat{r}$, $\mu_{\text{em}} = \hat{k}_{\text{em}} \cdot \hat{r}$. They take the range

$$\sqrt{1 - \frac{1}{x^2}} \leq \mu \leq 1; \quad -1 \leq \mu_{\text{em}} \leq 1. \quad (63)$$

Primed quantities are measured in the rest frame of a scattering charge.

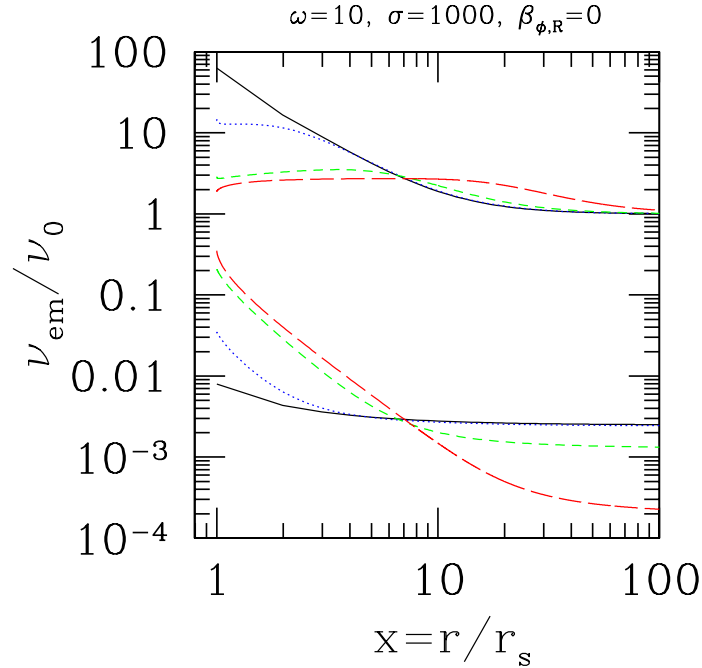


FIG. 8.— Maximum frequency of scattered photons (upper curves) and minimum frequency (lower curves), as a function of radius, in a strongly magnetized spherical wind ($\sigma = 10^3$). Compactness of photon source at $x = 1$: $\chi_s = 1$ (solid black); $\chi_s = 10^2$ (dotted blue); $\chi_s = 10^4$ (short-dashed green); $\chi_s = 10^6$ (long-dashed red).

A scattered photon reaches the maximum frequency

$$\nu_{\text{em,max}} = \frac{1 - \beta\mu_{\text{min}}}{1 - \beta}\nu_0 \simeq \left(1 + \frac{\Gamma^2}{x^2}\right)\nu_0 \quad (x, \Gamma \gg 1). \quad (64)$$

Hence the scattered spectrum develops a significant tail at frequencies above ν_0 if the outflow has a Lorentz factor $\Gamma \gtrsim \Gamma_{\text{eq}}$ [equation (32)]. This non-thermal tail is more pronounced at lower values of the compactness χ_s , where the Lorentz force dominates the acceleration of the flow. The scattered spectrum also extends to a low frequency $\nu_{\text{em,min}} = [(1 - \beta)/(1 + \beta)]\nu_0 \sim \nu_0/4\Gamma^2$. Sample profiles of $\nu_{\text{em,max}}$ and $\nu_{\text{em,min}}$ are given in Figure 8, and the asymmetry of the rest frame photon flux in Figure 9.

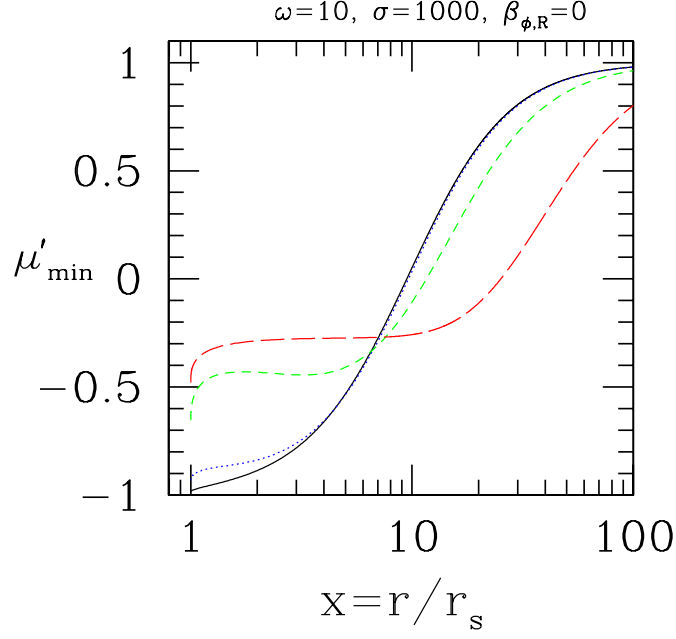


FIG. 9.— Asymmetry of the target photon distribution in the bulk frame of the outflow, represented by the minimum direction cosine of the photons μ' , as a function of radius. μ' is measured with respect to the flow direction, and is larger than the plotted value at very low frequencies [equation (77)]. Compactness of photon source at $x = 1$: $\chi_s = 1$ (solid black); $\chi_s = 10^2$ (dotted blue); $\chi_s = 10^4$ (short-dashed green); $\chi_s = 10^6$ (long-dashed red).

The frequency ν_{em} of the emitted photon is hardest in the flow direction. Softer photons are emitted off this axis, and also see a larger optical depth to scattering. In a spherically symmetric outflow, a photon emitted at radius r sees a scattering depth

$$\tau_{\text{es}}(r, \mu_{\text{em}}) = \frac{\sigma_T}{c} \frac{d\dot{N}}{d\Omega} \int_r^\infty [1 - \beta(r_2)\mu(r_2)] \frac{dr_2}{\beta(r_2)\mu(r_2)r_2^2}. \quad (65)$$

The direction cosine evolves from the emission radius r to $r_2 > r$ according to

$$1 - \mu(r_2)^2 = \left(\frac{r}{r_2}\right)^2 (1 - \mu_{\text{em}}^2) \quad (r_2 > r). \quad (66)$$

It is straightforward to calculate the emergent photon spectrum by a Monte Carlo method. The direction cosines of the input photons are drawn randomly from the uniform distribution (63) at $x = 1$. The optical depth $\Delta\tau_{\text{es}}$ to the first (next) scattering is determined by randomly picking $1 - e^{-\Delta\tau_{\text{es}}}$, followed by a step-by-step integration of τ_{es} along the ray. Scattering is performed in the rest frame of the cold flow, by transforming $\mu' = (\mu - \beta)/(1 - \beta\mu)$, picking rest frame scattering angles θ'_s, ϕ'_s with respect to this axis, and then determining the direction cosine of the outgoing photon via $\mu'_{\text{em}} = \mu' \cos\theta'_s + (1 - \mu'^2)^{1/2} \sin\theta'_s \cos\phi'_s$. The photon escapes if $\Delta\tau_{\text{es}}$ exceeds the total optical depth along the ray. Working in spherical symmetry, we record the frequency but not the direction of the outgoing photon.

6.2. Linear Flow Profile

To illustrate some of the main effects, we show in Figure 10 the spectrum resulting from an outflow with a simple linear profile $\Gamma(r) = 5(r/r_s)$, and various values of the scattering depth experienced by the most obliquely propagating photons. In this case, the bulk frame of the seed photons moves at a somewhat lower Lorentz factor than the magnetofluid, $\Gamma_{\text{slow}} \sim 0.2\Gamma$. The scattered spectrum therefore peaks well above the seed frequency, $\nu_{\text{em,max}} \sim 30\nu_0$ [equation (64)], driven by bulk Comptonization.

First consider the output from a monochromatic source spectrum (the black lines in Figure 10). The output spectrum is fairly flat, $F_\nu \sim \nu^{0.5}$, over a decade in frequency below the peak, steepening to $F_\nu \sim \nu$ at $\nu \sim \nu_0$. The scattered photons see a small optical depth (suppressed by a factor $\sim (\Gamma_{\text{slow}}/\Gamma)^2$ down to fairly low frequencies, where the slope approaches a Rayleigh-Jeans value.

As the optical depth of the seed photons is increased, the spectrum steepens slightly at high frequencies. The spectra in Figure (10) are labelled by the optical depth seen by seed photons at the maximum angle $\theta_s \sim (r/r_s)^{-1}$ and minimum direction cosine $\mu_{\text{min}} \simeq 1 - \theta_s^2/2$. Requiring that $\tau_{\text{es}}(r_s, \mu_{\text{min}}) \gtrsim 1$ allows the radial optical depth to remain small if $\Gamma \cdot \theta_s \gg 1$:

$$\tau_{\text{es}}(r_s, \mu_{\text{min}}) \sim [1 + \Gamma^2(r_s)] \tau_{\text{es}}(r_s, 1) \Rightarrow \tau_{\text{es}}(r_s, 1) \gtrsim \frac{1}{1 + \Gamma^2(r_s)}. \quad (67)$$

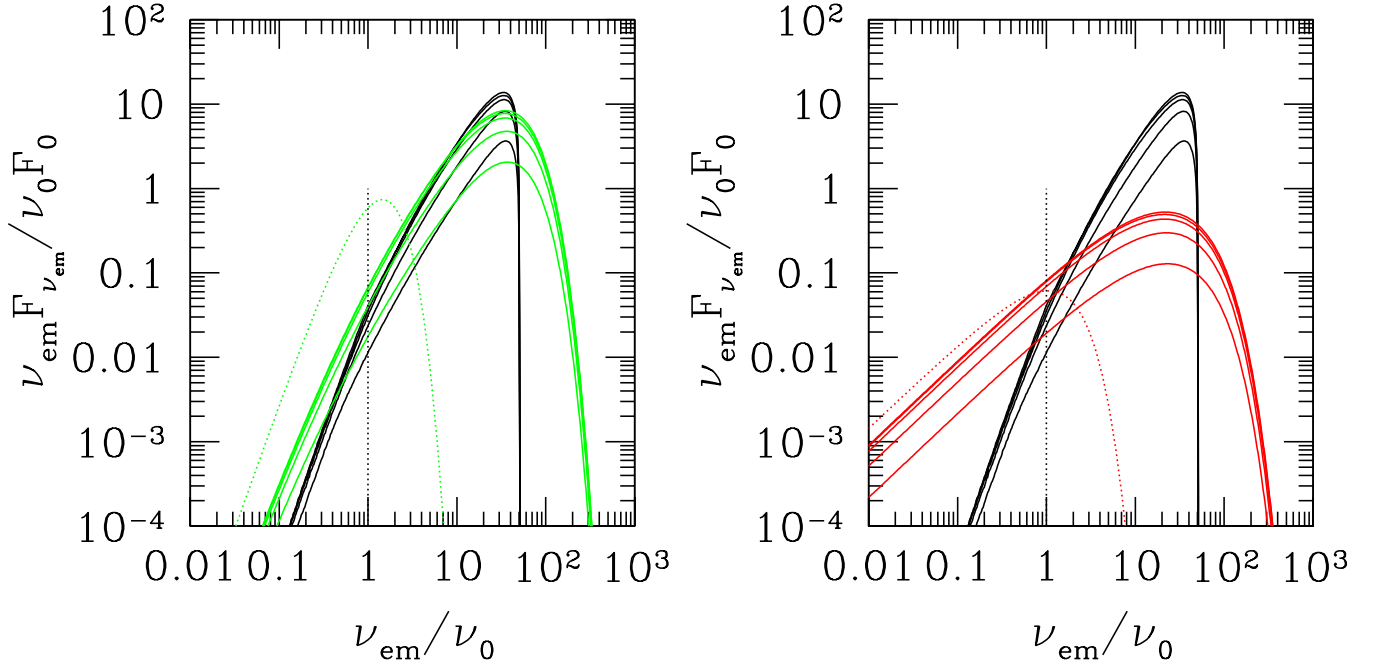


FIG. 10.— Spectrum of scattered photons emerging from a spherical outflow with a simple profile $\Gamma(r) = 5(r/r_s)$, obtained by direct Monte Carlo integration. Optical depth (67) of the off-axis photons is 0.3, 1, 3, 10, 30 from bottom to top, corresponding to optical depths $\lesssim 1$ after scattering at frequencies $\gtrsim \nu_0$. Unscattered source photons not included (see Figure 11 for comparison). Black lines: monochromatic source spectrum. *Left panel:* black-body photon source (green lines). *Right panel:* GRB-like source spectrum (red lines), $F_\nu \sim \text{const} \times e^{-h\nu/kT_0}$ (the low-frequency half of the Band function extended to higher frequencies). In both panels, the source spectrum is the dotted curve.

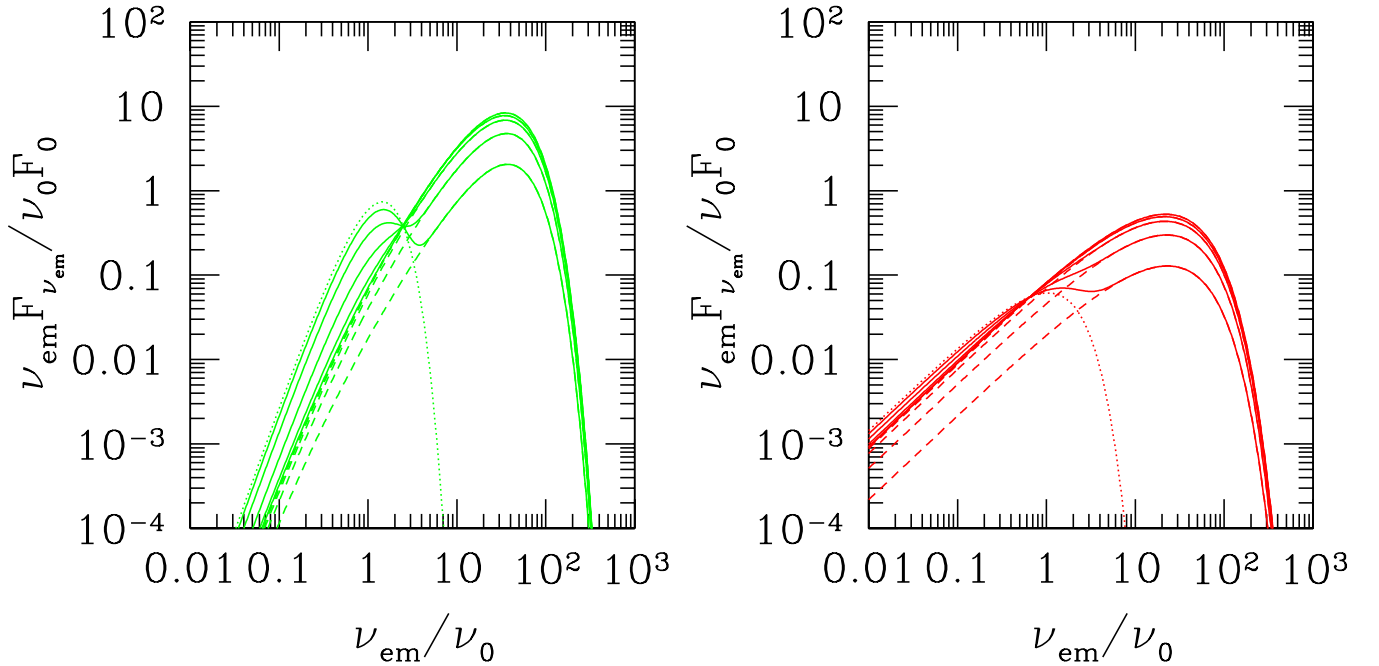


FIG. 11.— Solid curves: same as Figure 10, but adding in the unscattered component of the source spectrum. The scattered spectrum dominates near the seed blackbody peak when the off-axis optical depth $\tau_{\text{es}}(r_s, \mu_{\text{min}}) \gtrsim 10$. Dashed curves: only scattered photons included.

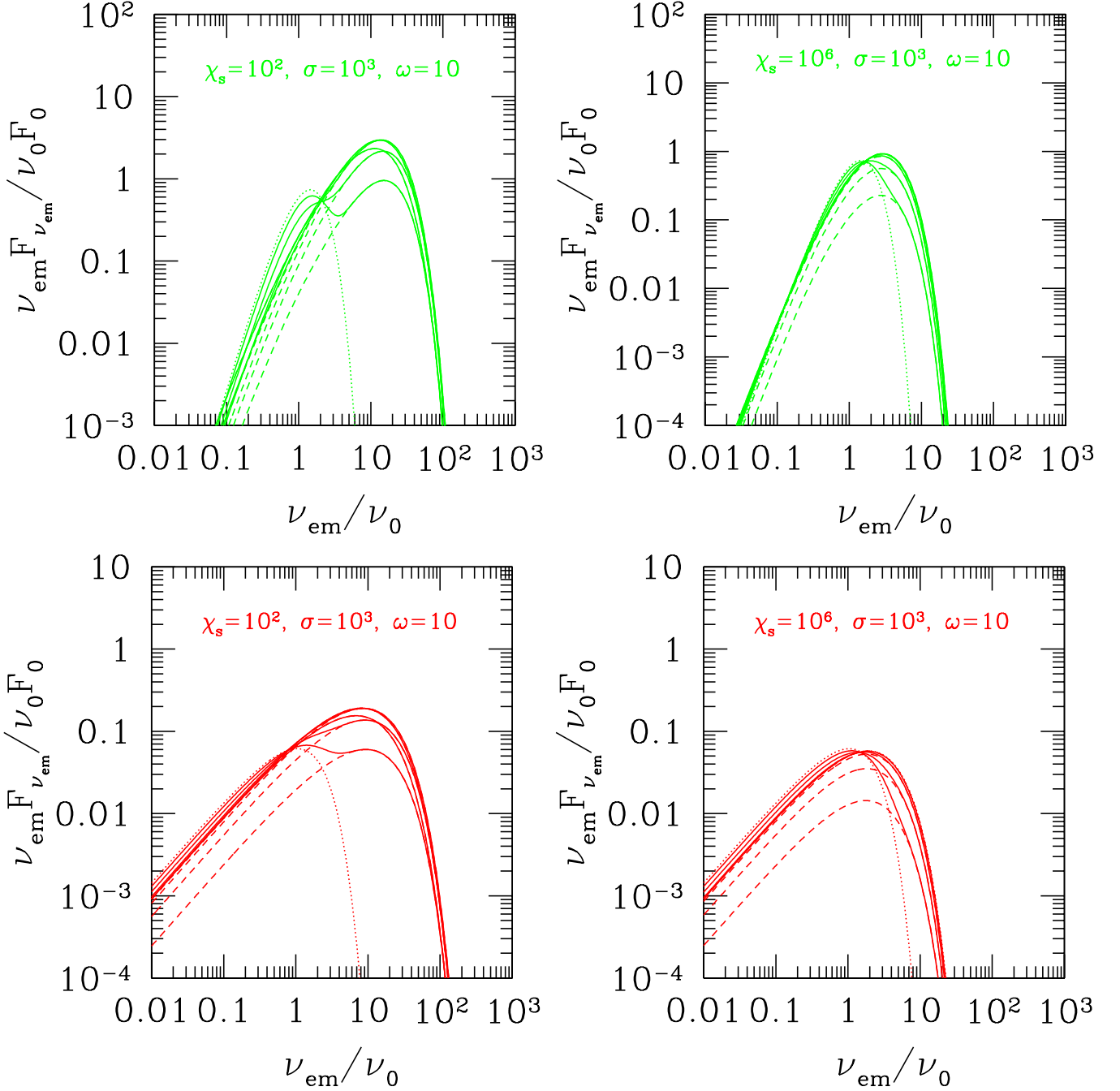


FIG. 12.— Total spectrum of photons emerging from a hot electromagnetic outflow ($\sigma = 10^3$) with a blackbody source of compactness $\chi_s = 10^2$ (left panel) and $\chi_s = 10^6$ (right panel). Flow profile shown in Figure 3. Curves from bottom to top have off-axis optical depth (67) equal to 0.3, 1, 3, 10, 30. Increasing $\tau_{\text{es}}(r_s, \mu_{\text{min}})$ implies that the outflow moves closer to the equilibrium value Γ_{eq} at the transparency radius, hence the steeper high-frequency spectrum. Dashed spectra do not include unscattered source radiation.

6.3. Generalization to Blackbody and Other Thermal Seeds

It is straightforward to calculate the output spectrum for a broadband source with spectrum $F_{\nu_0}(\nu_0)$ via

$$F_{\nu_{\text{em}}}(\tilde{\nu}_{\text{em}}) \rightarrow \int \frac{F_{\nu_0}(\nu'_0)}{F_0} F_{\nu_{\text{em}}} \left(\frac{\nu_{\text{em}}}{\nu'_0} \right) \frac{d\nu'_0}{\nu'_0}. \quad (68)$$

Here $F_{\nu_{\text{em}}}(\tilde{\nu}_{\text{em}})$ is the Greens function response (79) of the scattering outflow to a line photon source.

The result for a blackbody seed is shown in the left panel of Figure 10, and for a thermal seed with a GRB-like spectrum at low frequencies, $F_{\nu} = \text{constant} \times e^{-h\nu/kT_0}$, in the right panel.⁴ In both cases, the seed temperature is normalized so that F_{ν} peaks at

⁴ This corresponds to the low-frequency half of the Band function (Band et al. 1993). The high-frequency power-law tail of the observed GRB spectrum must

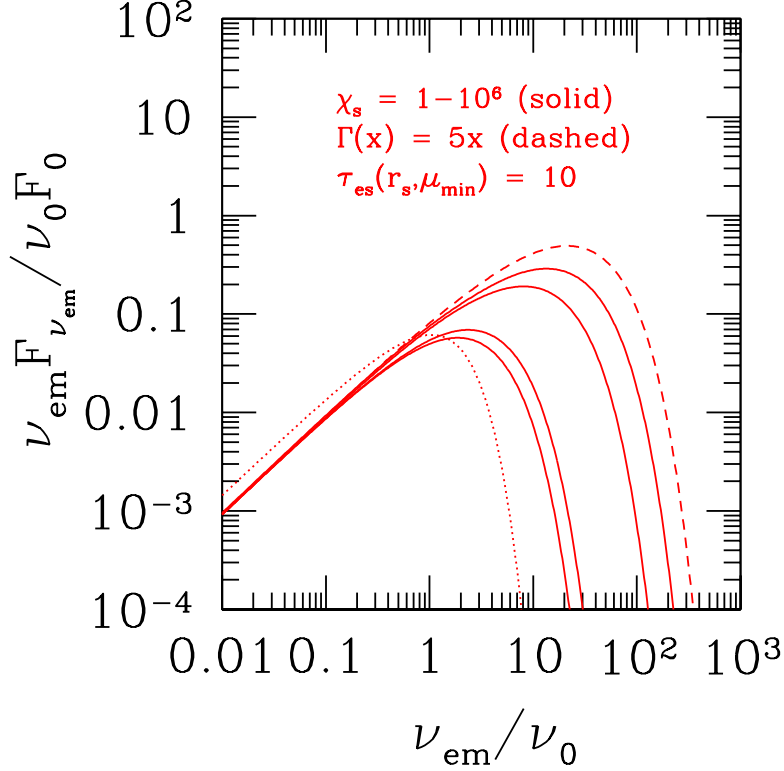


FIG. 13.— Same as Figure 12, with a GRB-like photon source (dotted curve), for a range of compactness $\chi_s = 1, 10^2, 10^4, 10^6$ (solid curves, softening at high frequencies with increasing compactness). Dashed line shows result for linear flow profile, $\Gamma(x) = 5x$. Outflow has a fixed off-axis optical depth $\tau_{\text{es}}(r_s, \mu_{\text{min}}) = 10$. See Figure 3 for corresponding flow profiles.

$\nu = \nu_0$. In the second case, the upscattered portion of the spectrum at $\nu > \nu_0$ connects smoothly with the seed spectrum at $\nu < \nu_0$.

One can also add in the source spectrum, appropriately attenuated,

$$F_{\nu_0} \rightarrow 2\pi \int I_{\nu_0} \exp[-\tau_{\text{es}}(r_s, \mu)] d\mu \simeq \frac{1 + \Gamma^{-2}(r_s)}{\tau_{\text{es}}(r_s, \mu_{\text{min}})} \left\{ \exp[-\tau(r_s, 1)] - \exp[-\tau(r_s, \mu_{\text{min}})] \right\} F_{\nu_0}, \quad (69)$$

where we have made use of the small-angle approximation (72) to the scattering depth. The effect is shown in Figure 11. The seed blackbody peak is apparent if the seed photons see a maximum optical depth $\tau(r_s, \mu_{\text{min}}) \sim 1$, and helps to extend the low-energy tail for $\tau(r_s, \mu_{\text{min}}) \sim 3$. It is subdominant for larger optical depths.

6.4. Results for Radiatively Driven MHD Winds

In Figures 12-15 we show spectra calculated using the outflow profiles obtained in Section 5, with flow parameters $\sigma = 1000$, $\omega = 10$. A distinct feature of the spectra is a prominent high energy tail appearing in outflows with moderate $\chi_s \lesssim 10^3$ – compare the spectra for $\chi_s = 10^2$ and 10^6 in Figure 12. At low compactness, the outflow acceleration is dominated by MHD forces, and $\Gamma \gg \Gamma_{\text{eq}}$ at the base of the outflow. When the acceleration is dominated by radiation pressure, increasing the optical depth only causes small changes in the peak of the scattered spectrum (as for $\chi_s = 10^6$). A direct comparison of outflows with a range of χ_s is made in Figure 13.

The spectral index of the $\chi_s = 10^2$ outflow is shown in Figure 14, for both blackbody and GRB-like seed spectra. As the optical depth at the base of the outflow increases, the cutoff frequency drops and the spectrum softens. In the blackbody case, the low-energy tail has a fairly constant, Rayleigh-Jeans slope, becoming slightly steeper at high compactness, as discussed in Section 6.5.

The decomposition of the output spectrum into the components emitted at different radii is shown in Figure 15. The contribution from large radius is in the optically thin regime, and has a harder spectrum than the (dominant) contribution near the photosphere. The overall normalization of the spectrum remains essentially constant, $F_{\nu_{\text{em}}} \sim F_0$, at $\nu_{\text{em}} \sim \nu_0$ when $\tau_{\text{es}}(r_s, \mu_{\text{min}}) \gtrsim 1$.

6.5. Low-Frequency Spectral Slope

Here we examine in more detail the effect that radiation transfer near a relativistic photosphere will have on the low-frequency spectrum. A Rayleigh-Jeans spectral slope arises from side scattering a monochromatic source in a locally spherical outflow, and is therefore maintained for a black body source (Section 6.3). The optical depth of low-frequency photons scales as $\tau_{\text{es}}(r, \theta_{\text{em}}) \propto \theta_{\text{em}}^2 \propto \Gamma^{-2} \nu_{\text{em}}^{-1}$ and emission time $t \propto \nu_{\text{em}}^{-1}$ for photons emitted off the axis to the observer. The increase in optical depth also

then result from further upscattering by a process not considered in this paper.

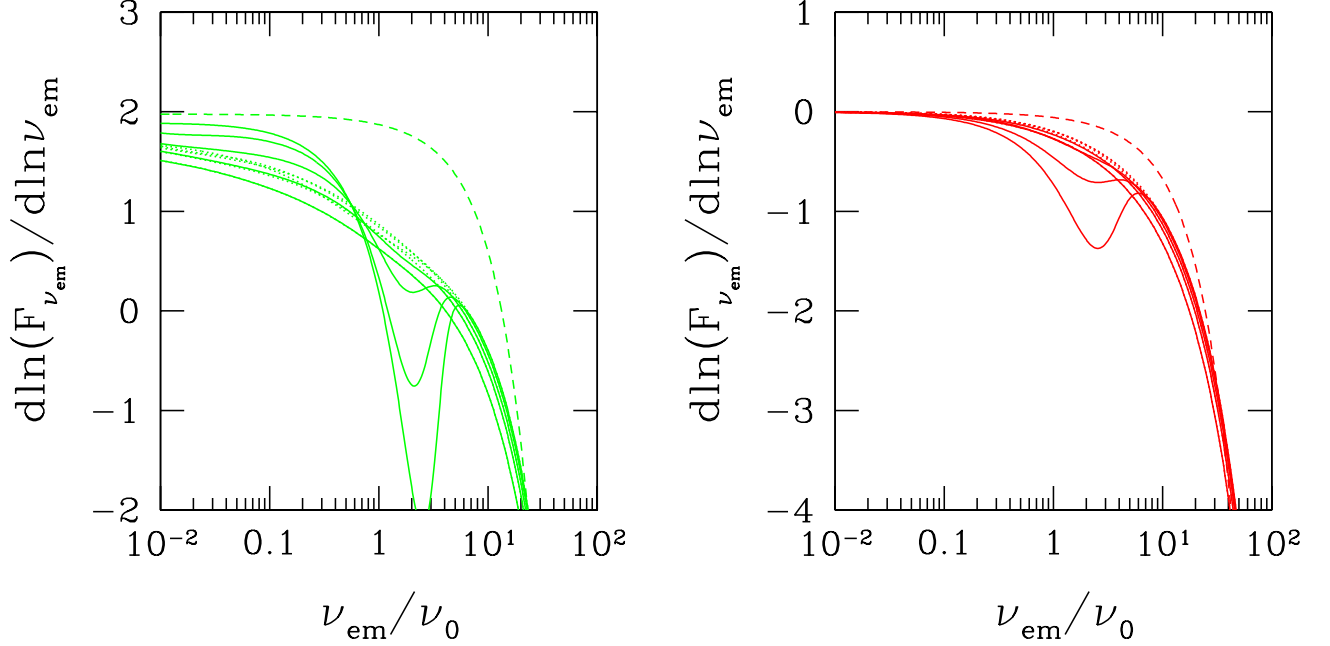


FIG. 14.— *Left panel*: Slope $d \ln(F_{\nu}) / d \ln \nu$ of the spectra displayed in Figure 12 (blackbody source), showing a flat spectrum just below the scattered peak, steepening to a Rayleigh-Jeans slope at low frequencies. Solid lines: photon source attenuated by scattering added to the scattered spectrum. Dotted line shows blackbody, shifted arbitrarily in peak frequency for comparison. *Right panel*: Same outflow, but now a GRB-like photon source. Dotted line shows source, shifted in peak frequency. See text for discussion.

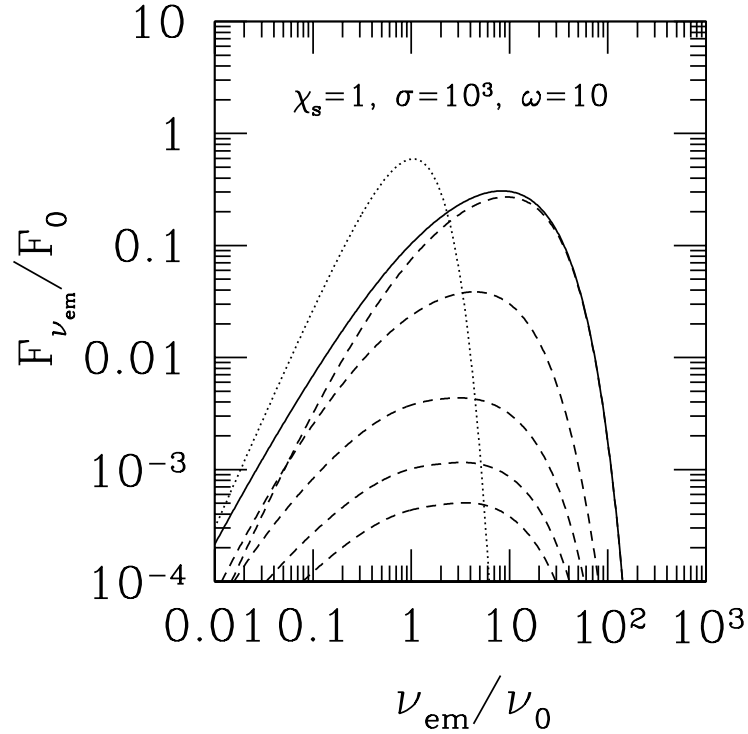


FIG. 15.— Spectrum of scattered blackbody photons in outflow with $\chi_s = 1$, $\sigma = 10^3$, $\omega = 10$, and $\tau_{\text{es}}(r_s, \mu_{\text{em}} = 1) = 10$, with the contributions from different radii separated out. Dashed curves show photons whose radius of last scattering lies in the range $1 < x < 10^{0.5}$, $10^{-0.5} < x < 10$, $10 < x < 10^{1.5}$, $10^{1.5} < x < 10^2$, $x > 10^2$. Solid curve: total scattered spectrum.

pushes the off-axis photosphere out to a radius $r_\tau(\nu_{\text{em}}) \propto \Gamma^{-2} \nu_{\text{em}}^{-1}$, where the rate of scatterings in a volume $\sim r_\tau^3$ is proportional to $(1-\beta)(\Gamma\rho)n_\gamma \propto \Gamma^{-2} r_\tau(\nu_{\text{em}})^{-1} \propto \nu_{\text{em}}$. In the optically thin regime, one therefore finds a low-frequency spectrum $F_{\nu_{\text{em}}} \propto t^{-1} \propto \nu_{\text{em}}$, which hardens to $F_{\nu_{\text{em}}} \propto \nu_{\text{em}}^2$ if every frequency is emitted from its photosphere.

It is also worth examining briefly how this result for a steady outflow would be modified in the case where the outflow is impulsive. Consider a slightly simpler situation in which the seed photons flow radially (and are monochromatic). Then the frequency of the outgoing photon is purely a function of scattering angle, and we can consider the number of photons scattered the bulk frame of the magnetofluid in a time interval dt' ,

$$d^2 N_\gamma = n'_{\gamma 0} c \frac{d\sigma_T}{d\mu'_{\text{em}}} d\mu'_{\text{em}} dt'. \quad (70)$$

Here $n'_{\gamma 0} \sim n_\gamma/\Gamma$ is the bulk frame photon density, and the differential scattering cross section varies mildly with the rest-frame scattering angle. Since $\nu_{\text{em}}/\nu_0 = (1-\beta)/(1-\beta\mu_{\text{em}}) = \Gamma^2(1-\beta)(1+\beta\mu'_{\text{em}})$, we have

$$\frac{d^2 N_\gamma}{d\tilde{\nu}_{\text{em}} dt'} = \frac{n'_{\gamma 0} c}{\Gamma^2 \beta (1-\beta)} \frac{d\sigma_T}{d\mu'_{\text{em}}}. \quad (71)$$

The observed arrival time of a photon depends on emission angle and therefore frequency, $dt_{\text{obs}} = \Gamma(1-\beta\mu_{\text{em}})dt' = \tilde{\nu}_{\text{em}}^{-1} \Gamma(1-\beta)dt'$. But integrating over the entire history of a pulse, the total number of photons emitted is $dN_\gamma/d\ln\nu_{\text{em}} \propto \nu_{\text{em}}$. At very low frequencies, one must compensate for the expanded photosphere and reduced scattering rate, as outlined above.

6.6. Semi-analytic Approximation to the Spectrum

In the Monte Carlo evaluation of the scattered spectrum, we tested a simplified evaluation of the optical depth integral, using the small-angle approximation and assume linear growth of the Lorentz factor, $\Gamma(r_2) = (r_2/r)\Gamma(r) \gg 1$. Then equation (65) becomes

$$\tau_{\text{es}}(r, \mu_{\text{em}}) \simeq \frac{\sigma_T}{6cr} \frac{d\dot{N}}{d\Omega} \left[\frac{1}{\Gamma^2(r)} + \theta_{\text{em}}^2 \right]. \quad (72)$$

The output spectra are hard to distinguish from those displayed in Figures (10), (11).

It is also useful to work out the spectrum of singly-scattered photons in the case where the seed photons see a small to modest optical depth. Since the matter is cold, it is simplest first to transform into its rest frame and consider the power scattered into solid angle $d\Omega'_{\text{em}}$,

$$\frac{d^3 E'}{d\nu'_{\text{em}} d\Omega'_{\text{em}} dt'} = \frac{3\sigma_T}{16\pi} \int I'_{\nu'} \left[1 + (\hat{k}' \cdot \hat{k}'_{\text{em}})^2 \right] d\Omega'. \quad (73)$$

The rest-frame frequency and spectral intensity are $\nu' = \nu_0/\Gamma(1+\beta\mu')$ and $I'_{\nu'} = I_\nu/[\Gamma(1+\beta\mu')]^3$. One sees in Figure 9 that the radiation field flows both forward and backward in the bulk frame close to the engine. At large distances the radiation field continues to collimate even as the Γ saturates, and $I'_{\nu'}$ is concentrated in the forward (anti-radial) direction.

The power of the scattered radiation from a single charge is

$$\begin{aligned} \frac{d^2 E}{d\nu_{\text{em}} dt} &= \int \frac{1}{\Gamma} \frac{d^3 E'}{d\nu'_{\text{em}} d\Omega'_{\text{em}} dt'} d\Omega'_{\text{em}} \\ &= \frac{3\sigma_T}{16\pi} \int d\Omega' d\Omega'_{\text{em}} \frac{I_0 \nu_0}{\Gamma^4 (1+\beta\mu')^3} \delta\left(\frac{1+\beta\mu'}{1+\beta\mu'_{\text{em}}} \nu_{\text{em}} - \nu_0\right) \left[1 + (\hat{k}' \cdot \hat{k}'_{\text{em}})^2 \right]. \end{aligned} \quad (74)$$

Using

$$\int d\phi' d\phi'_{\text{em}} \left[1 + (\hat{k}' \cdot \hat{k}'_{\text{em}})^2 \right] = 2\pi^2 \left[3 + 3\mu'^2 \mu'_{\text{em}}{}^2 - \mu'^2 - \mu'_{\text{em}}{}^2 \right] \quad (75)$$

gives

$$\frac{d^2 E}{d\nu_{\text{em}} dt} = \frac{3\pi\sigma_T I_0 \nu_0}{8 \beta \Gamma^4} \tilde{\nu}_{\text{em}} \int d\mu' \frac{3 + 3\mu'^2 \mu'_{\text{em}}{}^2 - \mu'^2 - \mu'_{\text{em}}{}^2}{(1+\beta\mu')^2}, \quad (76)$$

where $\mu'_{\text{em}} = \mu'_{\text{em}}(\mu', \tilde{\nu}_{\text{em}})$ from equation (62). The range of integration over μ' is restricted if $\tilde{\nu}_{\text{em}} > 1$. Since $1+\beta\mu' = (1+\beta\mu'_{\text{em}})/\tilde{\nu}_{\text{em}}$, we have $(1-\beta)/\tilde{\nu}_{\text{em}} \leq 1+\beta\mu' \leq (1+\beta)/\tilde{\nu}_{\text{em}}$, and more generally

$$\max \left[\frac{1-\beta}{\tilde{\nu}_{\text{em}}}, \frac{1}{\Gamma^2(1-\beta\mu_{\text{min}})} \right] \leq 1+\beta\mu' \leq (1+\beta) \min \left(1, \frac{1}{\tilde{\nu}_{\text{em}}} \right). \quad (77)$$

The flux of scattered radiation measured at a large distance is

$$F_{\nu_{\text{em}}}(r) = \frac{1}{r^2} \int_0^\infty \frac{dr}{\beta(r)c} \frac{d\dot{N}}{d\Omega} \frac{d^2 E}{d\nu_{\text{em}} dt}. \quad (78)$$

Normalizing to the incident radiation flux $F_0 = \pi I_0 \nu_0 / x^2$, gives

$$\frac{F_{\nu_{\text{em}}}}{F_0} = \frac{3\sigma_T}{8cr_s} \frac{d\dot{N}}{d\Omega} \tilde{\nu}_{\text{em}} \int d\mu' dx \frac{3 + 3\mu'^2 \mu'_{\text{em}}{}^2 - \mu'^2 - \mu'_{\text{em}}{}^2}{\Gamma^4 \beta^2 (1 + \beta \mu')^2}. \quad (79)$$

Following equation (72), the prefactor can be written as

$$\frac{3\sigma_T}{8cr_s} \frac{d\dot{N}}{d\Omega} = \frac{9}{4} \Gamma^2(r_s) \tau_{\text{es}}(r_s, 1). \quad (80)$$

7. SUMMARY AND CONCLUSIONS

We have considered a very luminous and strongly magnetized outflow outside its scattering photosphere. The outflow is accelerated to a high Lorentz factor by a combination of the Lorentz force (which acts in a cold MHD flow) and the radiation scattering force (dominant in thermal fireballs). A range of radiation intensities is considered, extending from an almost cold flow to one in which the radiation and magnetic Poynting fluxes are comparable. The calculations described in this first paper assume that the poloidal magnetic field is strictly monopolar, which results in a near degeneracy between magnetic pressure gradient and curvature forces. Similar solutions will obtain for any part of an MHD outflow in which the magnetic flux surfaces are unfavorably curved and the Lorentz force remains weak. The opposing case, corresponding to a flared jet that breaks out of a confining medium, is examined in detail in paper II.

The radiation force dominates the acceleration if the compactness $\chi \gtrsim \sigma$ at the photosphere. This inequality is easily satisfied if the outflow is optically thick near the engine: one has $\chi(r_\tau) \sim 6\Gamma^2(r_\tau)\sigma$ in an outflow with comparable Poynting and photon energy fluxes. Radiative driving is especially efficient beyond the fast critical point, even though the magnetic field dominates the inertia of the outflow. The solutions we obtain for high radiation intensities can easily be rescaled to an outflow with relativistic bulk motion at a displaced photosphere: then the flow profile $\Gamma(r)$ is linear in the inner parts of the outflow at both large and small scattering depths.

We have considered the imprint of bulk Compton scattering on a photon seed with an exponential, high-frequency spectral cutoff. The spectrum is strongly modified when the radiation compactness is low enough that outward acceleration is dominated by the Lorentz force *and* the seed photon beam is wider than the Lorentz cone of the magnetofluid. In this situation, the magnetofluid is pushed quickly to a high Lorentz factor outside its photosphere, where it feels a strong photon drag. Then the output spectrum extends above the seed peak frequency, with its low-frequency part depending on the shape of the seed. In the case of a blackbody seed, the spectral slope in between the seed thermal peak and the scattered peak is softer than Rayleigh-Jeans, but harder than is typical of GRBs at low frequencies.

We have also considered a seed spectrum $F_\nu \sim \text{const} \times e^{-h\nu/kT_0}$, representing the low-frequency part of the Band function absent the high-frequency tail. In that case, the scattered spectrum extends the flat portion of the seed spectrum upward in frequency. For both types of seed spectrum, the residual amplitude of the seed thermal peak that persists in the transmitted spectrum depends on the optical depth. A seed photon beam that is much wider than the Lorentz cone of the magnetofluid sees a large optical depth (compared with the optical depth of the more strongly beamed scattered photons), which means that the transmitted thermal peak is relatively weak. In the context of GRBs, the angular broadening of the seed photons could result from scattering by a second, slower component of the outflow that is swept up at the head of the jet (Thompson 2006).

In principle, no fine tuning of the optical depth surface is needed to make radiative and MHD acceleration competitive near the photosphere. The effective magnetization is much reduced below the photosphere, where the stress-energy of the photons couples to the matter and thence to the magnetic field: $\sigma_{\text{eff}} \sim L_p/L_\gamma$. Once the radiation begins to stream freely, the outflow experiences both a rapid increase in magnetization, and a strong outward force from the self-collimating radiation field. This effect is examined in detail in Paper II.

7.1. Connection with GRBs

At first sight, one might associate the high-energy tail of the scattered photon spectrum with the observed high-energy tails of GRBs, and the seed photon energy with the observed spectral peak energy E_{pk} . But the calculated spectrum is relatively hard compared with the high-energy tails of GRBs, and it is limited in spectral width.

Instead it appears more promising to identify the high-energy peak of the scattered spectrum with the measured E_{pk} – at least in some bursts or possibly some phases of the burst emission. Then an additional source of dissipation, which is left out of our calculations, is needed to generate the high-energy tail. The seed thermal photons, generated deep in the outflow, provide a buffer that suppresses bursts with low E_{pk} , but upscattering allows a range of *higher* E_{pk} values. We leave open here the nature and origin of the low-frequency seed spectrum, except to say that a hard Rayleigh-Jeans slope is by no means guaranteed if thermalization occurs at an intermediate optical depth.

In this context, it is worth recalling some features of the Amati et al. (2002) relation between E_{pk} and the apparent isotropic energy E_{iso} of GRBs. This relation is suggestive of jet breakout from the core of a Wolf-Rayet star (e.g. Thompson 2006), but it appears to represent a boundary in the $E_{\text{pk}}-E_{\text{iso}}$ plane. The observed bursts have E_{pk} lying on or above the Amati et al. line, with a strong deficit mainly below the line: for example, a significant proportion of BATSE burst spectra are too hard to be consistent with this relation, independent of the (unknown) redshift (Nakar & Piran 2005).

Evidence for a low frequency blackbody component has been found in some gamma-ray bursts (e.g. Axelsson et al. 2012). It is natural to try to accommodate such components in the present calculation, where the thermal seed should be partially transmitted. The measured soft blackbody component sits a factor $\sim 1/30$ below the burst peak, which requires a large broadening of the seed photons (by a factor $\sim \Gamma \theta_{\text{seed}} \sim 5$ in angle, where θ_{seed} is the angular width of the seed component). If the decrease in the peak

frequency during the burst evolution were due *mainly* to a drop in $\Gamma\theta_{\text{seed}}$, then one would expect to see a strong re-emergence of the seed thermal peak alongside the scattered peak, which is generally not observed. When considering the emission from relativistic outflows, one must always keep in mind the basic degeneracy between temporal and spectral degrees of freedom, and the angular degree of freedom. Therefore the presence of a soft thermal component in the spectrum may signal the presence of off-axis emission that does not, necessarily, interact with the emission zone of the harder component.

Finally, one should keep in mind that the scattered thermal radiation emitted by an electromagnetic outflow could represent a subcomponent of the burst emission, with some other non-thermal (e.g. synchrotron) process dominating (Pe'er et al. 2006; Zhang & Yan 2011). In that case, the photon field would have a smaller (but not necessarily negligible) influence on the outflow acceleration.

7.2. Alternative Acceleration Mechanisms for Strictly Radial Magnetized Outflows

We find that a hot electromagnetic outflow typically experiences a strong radiation force before it expands far enough that radial inhomogeneities become important. The acceleration of a static, bounded magnetic slab, studied by Granot et al. (2011), could be relevant for the later stages of impulsive GRB outflows, outside a radius $\sim c\Delta t$. But if a magnetized shell already moves relativistically at this radius, only a thin outer layer, comprising a fraction $\sim 1/2\Gamma^2$ of the shell, would experience a strong outward magnetic pressure gradient force. Its interaction with slower material, swept up from a Wolf-Rayet star or a preceding neutron-rich wind, must then be taken into account.

Other acceleration mechanisms have been suggested which depend on more complicated, non-ideal MHD effects, such as the creation of a (net) outward pressure gradient force by reconnection of a toroidal magnetic field (Drenkhahn & Spruit 2002). Zones of alternating B_ϕ , separated by current sheets, are indeed present in the force-free solution to the oblique rotator (Spitkovsky 2006), in a zone straddling the rotational equator. An active dynamo operating in a GRB engine could also lead to stochastic reversals in the wind magnetic field (Thompson 2006). But when the increase in flow inertia associated with particle heating and radiation is taken into account, we have argued that cancelling even half the magnetic flux leads only to mildly relativistic radial motion. Magnetic reconnection plays a more natural role in the GRB phenomenon by modifying the gamma-ray spectrum, via particle heating and stochastic bulk motions.

We thank the NSERC of Canada for financial support, and the referee for comments.

APPENDIX

ROTATING EMISSION SURFACE

The photon source rotates rapidly in some cases, e.g. a rapidly rotating star such as a millisecond magnetar, or the merged remnant of a white dwarf binary. We can approximate the effect of a rotating emission surface by setting

$$\beta_\phi \rightarrow \beta_\phi - \frac{\beta_{\phi,R}}{x} \quad (\text{A1})$$

in equations (28), and (29). Here $\beta_{\phi,R}$ is a constant representing the aberration of the outflowing photons at $r = r_s$ ($x = 1$). In this situation, plasma near the emission surface can more easily co-rotate with the radiation field while still being accelerated outward.

The value of $\beta_{\phi,R}$ depends on the type of source. One has $\beta_{\phi,R} \sim \Omega r_s/c \equiv \omega$ when the photons flow from the surface of a star of radius r_s through a transparent wind. On the other hand, if the outflow is optically thick in a narrow radial zone close to the engine, then one expects $\beta_{\phi,R} \sim (\Omega r_s/c)^{-1} \sim \omega^{-1}$ based on the conservation of angular momentum from the light cylinder out to the transparency surface ($x = 1$).

In a first approximation, rotation of the photon source makes only small changes to the profiles of Lorentz factor and angular momentum in the outflow. For completeness, we discuss some of the detailed changes that do result in the flow parameters at the fast point. These effects are largest in intense radiation fields with compactness $\chi_s > 4\sigma^{4/3}/\omega^2$. Then, as in our previous calculations with a non-rotating photon source (Section 4.4), the location of the critical point is determined by setting $\Gamma_c = \Gamma_{\text{eq}}(r)$ [equation (32)]. Corotation of the fluid and the radiation field implies

$$\beta_{\phi,c} \simeq \frac{\beta_{\phi,R}}{x_c}, \quad (\text{A2})$$

where $x_c \simeq \Gamma_c/3^{1/4}$. When $\beta_\phi \neq 0$, the fast speed (50) becomes

$$u^3 \simeq \sigma \left[1 + \Gamma^2 \frac{B_r^2}{B_\phi^2} (1 - \beta_\phi x \omega)^2 \right] \simeq \sigma. \quad (\text{A3})$$

At large compactness, the Lorentz factor and angular momentum at the critical point are given by

$$\Gamma_c \simeq \sigma^{1/3} \left(1 + \sqrt{3}(\omega^{-1} - \beta_{\phi,R})^2 \right)^{1/3}; \quad \mathcal{L}_c \simeq \frac{\Gamma_c}{\omega} \left[\beta_{\phi,R} \omega + \frac{\sigma^{2/3}}{\left(1 + \sqrt{3}(\omega^{-1} - \beta_{\phi,R})^2 \right)^{1/3}} \right] \quad (\text{large } \chi_s). \quad (\text{A4})$$

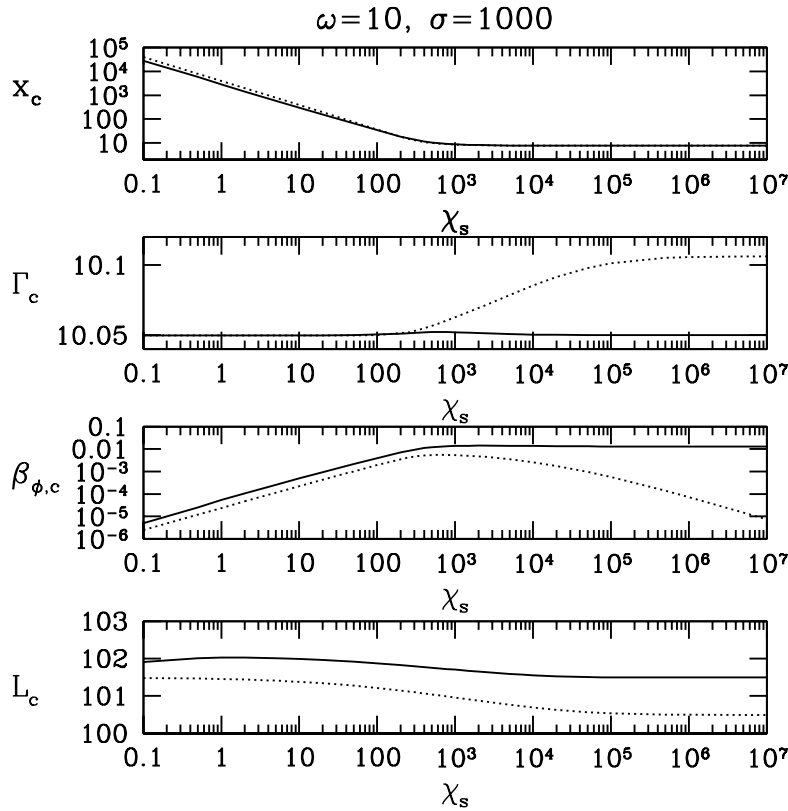


FIG. 16.— Effect of rotation of the photon source (compactness χ_s) on the properties of the fast critical point: radius x_c and flow variables Γ , β_ϕ and \mathcal{L} . Solid line: $\beta_{\phi,R} = 1/\omega = 0.1$ [equation (A1)]; dotted line: $\beta_{\phi,R} = 0$. Flow magnetization $\sigma = 10^3$.

One sees that the inertia added by the radial magnetic field can be significantly reduced when $\beta_\phi \simeq 1/x\omega$, that is when $\beta_{\phi,R} \simeq \omega^{-1}$.

A comparison of flow profiles with, and without, rotation of the photon source is made in Figure 16. There is little change in the critical point radius, but Γ_c remains close to $\sigma^{1/3}$ at all values of the compactness, since we have taken $\beta_{\phi,R} \simeq \omega^{-1}$. The magnetofluid rotates more rapidly near the critical point at large values of χ_s .

REFERENCES

- Amati, L., Frontera, F., Tavani, M., et al. 2002, *A&A*, 390, 81
Axelsson, M., Baldini, L., Barbiellini, G., et al. 2012, *ApJ*, 757, L31
Band, D., Matteson, J., Ford, L., et al. 1993, *ApJ*, 413, 281
Begelman, M. C., & Li, Z.-Y. 1994, *ApJ*, 426, 269
Beloborodov, A. M. 2002, *ApJ*, 565, 808
Beloborodov, A. M. 2010, *MNRAS*, 407, 1033
Beloborodov, A. M. 2011, *ApJ*, 737, 68
Beskin, V. S., Zakamska, N. L., & Sol, H. 2004, *MNRAS*, 347, 587
Blandford, R. D., & Znajek, R. L. 1977, *MNRAS*, 179, 433
Blandford, R. D., & Payne, D. G. 1982, *MNRAS*, 199, 883
Bucciantini, N., Metzger, B. D., Thompson, T. A., & Quataert, E. 2012, *MNRAS*, 419, 1537
Contopoulos, I. 2005, *A&A*, 442, 579
Dessart, L., Ott, C. D., Burrows, A., Rosswog, S., & Livne, E. 2009, *ApJ*, 690, 1681
Drenkhahn, G., & Spruit, H. C. 2002, *A&A*, 391, 1141
Ferraro, V. C. A. 1937, *MNRAS*, 97, 458
Ghisellini, G., Lazzati, D., Celotti, A., & Rees, M. J. 2000, *MNRAS*, 316, L45
Giannios, D. 2006, *A&A*, 457, 763
Giannios, D., & Spruit, H. C. 2007, *A&A*, 469, 1
Goldreich, P., & Julian, W. H. 1970, *ApJ*, 160, 971
Granot, J., Komissarov, S. S., & Spitkovsky, A. 2011, *MNRAS*, 411, 1323
Guess, A. W. 1962, *ApJ*, 135, 855
Goodman, J. 1986, *ApJ*, 308, L47
Kippenhahn et al. (1967) Kippenhahn, R., Weigert, A., Hofmeister, E. (1967): *Computing Stellar evolution*. *Meth. Comp. Phys.*, 7, 129
Kiusalaas, J. 2010, *Numerical Methods in Engineering with Python* (2nd ed.; New York: Cambridge University Press)
Lazzati, D., Morsony, B. J., & Begelman, M. C. 2011, *ApJ*, 732, 34
Li, Z.-Y., Begelman, M. C., & Chiueh, T. 1992, *ApJ*, 384, 567
London, R. A., & Flannery, B. P. 1982, *ApJ*, 258, 260
Lytikov, M., & Blandford, R. 2003, arXiv:astro-ph/0312347
MacFadyen, A. I., & Woosley, S. E. 1999, *ApJ*, 524, 262
Meszaros, P., & Rees, M. J. 1997, *ApJ*, 482, L29
McKinney, J. C. 2006, *MNRAS*, 368, L30
Metzger, B. D., Giannios, D., Thompson, T. A., Bucciantini, N., & Quataert, E. 2011, *MNRAS*, 413, 2031
Michel, F. C. 1969, *ApJ*, 158, 727
Nakar, E., & Piran, T. 2005, *MNRAS*, 360, L73
Panaitescu, A., & Kumar, P. 2002, *ApJ*, 571, 779
Pe'er, A., Mészáros, P., & Rees, M. J. 2006, *ApJ*, 642, 995
Pe'er, A. 2008, *ApJ*, 682, 463
Press, William H. and Teukolsky, Saul A. and Vetterling, William T. and Flannery, Brian P. 2007, *Numerical Recipes 3rd Edition: The Art of Scientific Computing* (3rd ed.; New York: Cambridge University Press)
Rhoads, J. E. 1999, *ApJ*, 525, 737
Shemi, A., & Piran, T. 1990, *ApJ*, 365, L55
Sikora, M., Begelman, M. C., & Rees, M. J. 1994, *ApJ*, 421, 153
Spitkovsky, A. 2006, *ApJ*, 648, L51
Tchekhovskoy, A., McKinney, J. C., & Narayan, R. 2009, *ApJ*, 699, 1789
Tchekhovskoy, A., Narayan, R., & McKinney, J. C. 2010, 15, 749
Thompson, C. 1994, *MNRAS*, 270, 480
Thompson, C. 2006, *ApJ*, 651, 333
Thompson, C., & Madau, P. 2000, *ApJ*, 538, 105
van Eerten, H., van der Horst, A., & MacFadyen, A. 2012, *ApJ*, 749, 44
Zhang, B., Fan, Y. Z., Dyks, J., et al. 2006, *ApJ*, 642, 354
Zhang, B., & Yan, H. 2011, *ApJ*, 726, 90